Influence of H2O and H2S on the Composition, Activity, and Stability of Sulfided Mo, CoMo, and NiMo Supported on MgAl2O4 for Hydrodeoxygenation of Ethylene Glycol

Dabros, Trine Marie Hartmann; Gaur, Abhijeet; Pintos, Delfina Garcia; Sprenger, Paul; Høj, Martin; Hansen, Thomas Willum; Studt, Felix; Gabrielsen, Jostein; Grunwaldt, Jan-Dierk; Jensen, Anker Degn

Published in:
Applied Catalysis A: General

Link to article, DOI:
10.1016/j.apcata.2017.12.008

Publication date:
2018

Document Version
Peer reviewed version

Accepted Manuscript

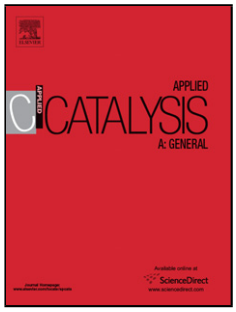

Title: Influence of H_2O and H_2S on the Composition, Activity, and Stability of Sulfided Mo, CoMo, and NiMo Supported on $MgAl_2O_4$ for Hydrodeoxygenation of Ethylene Glycol

Authors: Trine Marie Hartmann Dabros, Abhijeet Gaur, Delfina Garcia Pintos, Paul Sprenger, Martin Høj, Thomas Willum Hansen, Felix Studt, Jostein Gabrielsen, Jan-Dierk Grunwaldt, Anker Degn Jensen

PII: S0926-860X(17)30562-8
DOI: https://doi.org/10.1016/j.apcata.2017.12.008
Reference: APCATA 16488

To appear in: *Applied Catalysis A: General*

Received date: 2-10-2017
Revised date: 21-11-2017
Accepted date: 9-12-2017

Please cite this article as: Dabros TMH, Gaur A, Pintos DG, Sprenger P, Høj M, Hansen TW, Studt F, Gabrielsen J, Grunwaldt J-D, Jensen AD, Influence of H_2O and H_2S on the Composition, Activity, and Stability of Sulfided Mo, CoMo, and NiMo Supported on $MgAl_2O_4$ for Hydrodeoxygenation of Ethylene Glycol, *Applied Catalysis A, General* (2010), https://doi.org/10.1016/j.apcata.2017.12.008

Influence of H_2O and H_2S on the Composition, Activity, and Stability of Sulfided Mo, CoMo, and NiMo Supported on $MgAl_2O_4$ for Hydrodeoxygenation of Ethylene Glycol

Authors:

Trine Marie Hartmann Dabros[1], Abhijeet Gaur[2], Delfina Garcia Pintos[3], Paul Sprenger[2], Martin Høj[1], Thomas Willum Hansen[4], Felix Studt[3,5], Jostein Gabrielsen[6], Jan-Dierk Grunwaldt[2,5], Anker Degn Jensen[1*]

1) Department of Chemical and Biochemical Engineering, Technical University of Denmark (DTU), Søltofts Plads 229, Kgs. Lyngby, DK-2800 (Denmark).
2) Institute for Chemical Technology and Polymer Chemistry, Karlsruhe Institute of Technology (KIT), Engesserstraße 18/20, Karlsruhe, D-76131 (Germany).
3) SUNCAT Center for Interface Science and Catalysis, SLAC National Accelerator Laboratory, 2575 Sand Hill Road, Menlo Park, CA-94305 (USA).
4) Center for Electron Nanoscopy, Technical University of Denmark (DTU), Fysikvej 307, Kgs. Lyngby, DK-2800 (Denmark).
5) Institute of Catalysis Research and Technology, Karlsruhe Institute of Technology (KIT), Hermann-von-Helmholtz Platz 1, Eggenstein-Leopoldshafen, D-76344 (Germany).
6) Haldor Topsøe A/S, Haldor Topsøes Allé 1, Kgs. Lyngby, DK-2800 (Denmark).

*aj@kt.dtu.dk, Department of Chemical and Biochemical Engineering, Technical University of Denmark (DTU), Søltofts Plads 229, Kgs. Lyngby, DK-2800 (Denmark).

Graphical abstract

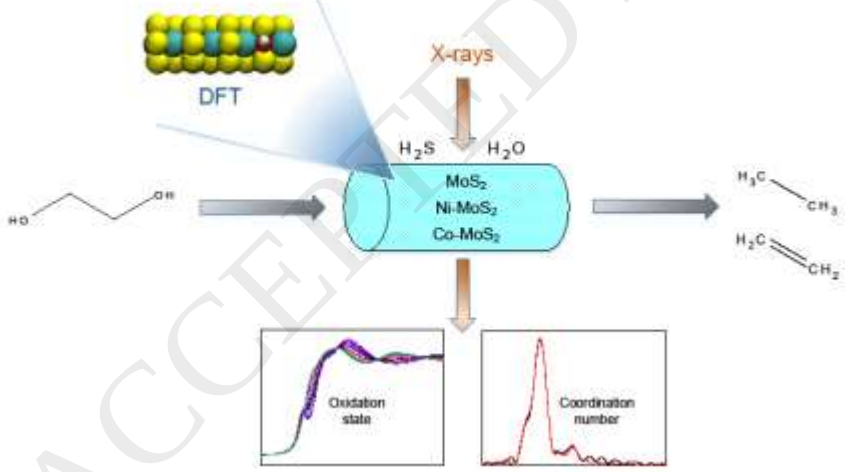

Highlights:

1) New insights into (Ni/Co)-MoS_2/$MgAl_2O_4$ catalysts for hydrodeoxygenation (HDO) of ethylene glycol showed high water tolerance and importance of promotion and H_2S level during HDO.
2) Catalyst HDO/cracking selectivity was >1.5 at 50-100 % conversion. Density functional theory indicated stabilization of the active edge by promotion and by increased H_2S partial pressure.
3) In-situ X-ray absorption spectroscopy unraveled a highly dispersed active phase, indicating strong support interaction and stabilization of the active molybdenum sulfide particles.
4) With these insights, catalyst formulations and operating conditions for catalytic hydropyrolysis of biomass or HDO of pyrolysis vapors can be optimized for production of green fuels.

Abstract

In this work, density functional theory (DFT), catalytic activity tests, and in-situ X-ray absorption spectroscopy (XAS) was performed to gain detailed insights into the activity and stability of MoS_2, Ni-MoS_2, and Co-MoS_2 catalysts used for hydrodeoxygenation (HDO) of ethylene glycol upon variation of the partial pressures of H_2O and H_2S. The results show high water tolerance of the catalysts and highlight the importance of promotion and H_2S level during HDO.

DFT calculations unraveled that the active edge of MoS_2 could be stabilized against S-O exchanges by increasing the partial pressure of H_2S or by promotion with either Ni or Co. The Mo, NiMo, and CoMo catalysts of the present study were all active and fairly selective for ethylene glycol HDO at 400 °C, 27 bar H_2, and 550-2200 ppm H_2S, and conversions of ≈ 50-100 %. The unpromoted Mo/$MgAl_2O_4$ catalyst had a lower stability and activity per gram catalyst than the promoted analogues. The NiMo and CoMo catalysts produced ethane, ethylene, and C_1 cracking products with a C_2/C_1 ratio of 1.5-2.0 at 550 ppm H_2S. This ratio of HDO to cracking could be increased to ≈

2 at 2200 ppm H_2S which also stabilized the activity. Removing H_2S from the feed caused severe catalyst deactivation. Both DFT and catalytic activity tests indicated that increasing the H_2S concentration increased the concentration of SH groups on the catalyst, which correspondingly activated and stabilized the catalytic HDO performance. In-situ XAS further supported that the catalysts were tolerant towards water when exposed to increasing water concentration with H_2O/H_2S ratios up to 300 at 400-450 °C.

Raman spectroscopy and XAS showed that MoS_2 was present in the prepared catalysts as small and highly dispersed particles, probably owing to a strong interaction with the support. Linear combination fitting (LCF) analysis of the X-ray absorption near edge structure (XANES) spectra obtained during in-situ sulfidation showed that Ni was sulfided faster than Mo and CoMo, and that Mo was sulfided faster when promoted with Ni. Extended X-ray absorption fine structure (EXAFS) results showed the presence of MoS_2 in all sulfided catalysts. Sulfided CoMo was present as a mixture of CoMoS and Co_9S_8, whereas sulfided NiMo was present as NiMoS.

Key words: Hydrodeoxygenation; DFT; molybdenum sulfide; XAS; bio-oil

1. Introduction

There is a need to produce energy from renewable sources to become less dependent on the depleting fossil resources and in order to minimize greenhouse gas (GHG) emissions as their effects on global warming are becoming more apparent [1].

Lignocellulosic biomass is a renewable carbon source that can be used for fuel production with minimum (potentially zero) carbon footprint [2–4]. It can be converted into bio-oil by fast pyrolysis,

which is a thermochemical degradation obtained by fast heating (700-10,000 °C/s) of biomass particles to ≈ 500 °C with short vapor residence times (<2s); typically in a fluid bed or cyclone reactor [5]. The elemental composition of bio-oil is similar to its parent biomass, but the volumetric energy density can be increased by a factor of >6 [6,7]. The lower heating value (LHV) of bio-oil (16.5-17.5 MJ/kg) is however less than half that of diesel and heavy fuel oil (40-43 MJ/kg) [8,9]. This is due to a high content of oxygen (32-50 wt%), which is present as sugar fragments, acids, aldehydes, ketones, furans, pyrans, phenols, guaiacols, and syringols [10–12]. Owing to the nature of these oxygenates, the oil is viscous, acidic, and unstable upon storage and heating. Additionally, the high polarity makes the oil immiscible with hydrocarbon fuels. Thus, the direct application of fast pyrolysis bio-oil as an engine fuel is highly challenged.

Bio-oil can be upgraded by catalytic hydrodeoxygenation (HDO), similar to hydrotreating [13]. HDO of condensed bio-oil is challenged by rapid catalyst deactivation and reactor plugging, which occurs upon reheating of the condensed oil [11,14–19]. This is mainly due to coking and polymerization of the very reactive cellulose and hemicellulose fragments in the bio-oil [20–22]. A different approach is in-situ HDO of the pyrolysis vapor, whereby the reactive compounds can be upgraded and stabilized before condensation. This could be achieved either via catalytic hydropyrolysis in a fluid bed reactor or by fixed bed HDO on the fast pyrolysis vapors before condensation [23,24]. For catalytic hydropyrolysis in a fluid bed (at ≈ 500 °C), the catalyst must be attrition resistant, and moderate activity is necessary in order to avoid severe cracking of the biomass into light gasses at elevated temperature.

Sulfide based catalysts, Ni- and Co-MoS_2/Al_2O_3, which are used as commercial hydrodesulfurization (HDS) catalysts, are active for HDO of bio-oil and model compounds showing promising activity and stability [17,25–35]. Compared to other catalyst systems such as reduced transition metal catalysts [11,36–38], sulfide catalysts are promising due to their moderate price and

tolerance against sulfur, which is inevitably present in bio-oil [8,39]. γ-Al_2O_3, which is a commonly applied support material [34,35], is however not tolerant against water, which is both present in bio-oil and formed during HDO, as it converts into boehmite [36,40].

Density functional theory (DFT) studies have indicated that exposure of MoS_2 to water vapor can lead to exchange of S with O at the active edge of MoS_2 and that promotion can stabilize the catalyst against these exchanges [26,41]. Co-feeding of H_2S is necessary to keep the catalyst in its active sulfide form [35,41–43] and to enhance the activity [41,44]. H_2S can however also inhibit the reaction [28,33,45], as it potentially saturates the coordinatively unsaturated sites (CUS), which are commonly accepted as active sites for oxygenate adsorption and deoxygenation [30,46–48]. Badawi et al. [41] reported that the state of the active edge can be controlled through the H_2O/H_2S ratio to avoid S-O exchanges, but the influence of water on the working catalyst has not been fully understood [44]. In order to optimize sulfide catalysts for HDO, a water tolerant support material should be chosen and the influence of H_2S and H_2O should be investigated experimentally; both in terms of HDO activity and catalyst structure.

In this work, MoS_2, Ni-MoS_2, and Co-MoS_2 clusters have been modeled with DFT to obtain insights into structural changes at the active edges under exposure to varying H_2O/H_2S ratios. MoS_2, Ni-MoS_2, and Co-MoS_2 supported on a water tolerant and attrition resistant $MgAl_2O_4$ spinel support were prepared and tested for the hydroconversion of ethylene glycol. Ethylene glycol was chosen as a simple model sugar fragment; representing the more reactive fraction of pyrolysis vapors. The influence of varying the feed concentration of H_2S was tested in catalyst activity tests with constant ethylene glycol feed. The evolution of the active sulfide phase in the catalysts was studied in-situ with X-ray absorption spectroscopy (XAS) in terms of X-ray absorption near edge structure (XANES) and extended X-ray absorption fine structure (EXAFS) spectroscopy. At first,

sulfidation rates were compared for the three catalysts. The influence of varying H_2O/H_2S ratios on the catalyst structure was furthermore investigated experimentally using in-situ XAS.

2. Experimental

2.1. Computational Details

Plane-wave DFT calculations were performed using the Quantum Espresso [49] code in combination with the BEEF-vdW [50] exchange correlation functional, as this functional has been shown to yield a reliable description of heats of formation of metal sulfide compounds [51]. The Brillouin zone was sampled using a 2x1x1 Monkhorst-Pack *k*-points set [52]. A kinetic energy cutoff of 500 Rydberg and a density cutoff of 5000 Rydberg were employed. Ultrasoft pseudopotentials were used to represent the ionic cores. The occupation of the Kohn-Sham states was smeared according to a Fermi-Dirac distribution with a Fermi temperature of k_BT = 0.1 eV, and energies were extrapolated to zero electronic temperature. Spin-polarization was considered for all calculations. The MoS_2, Ni-MoS_2, and Co-MoS_2 systems were studied using an infinite stripe model exposing both the M-edge and the S-edge [53]. The unit cell consisted of 4 metal atoms in both x and y direction. The slabs were separated by 8.6 and 14.8 Å in the y and z direction, respectively. Investigations of unpromoted MoS_2 were focused on the M-edge whereas the S-edge was considered for Ni and Co promoted MoS_2, with Ni and Co fully decorating the edge in each case. The phase diagram of the M-edge was constructed considering different coverages of S and H while keeping the S-edge unchanged. Likewise, phase diagrams of Ni and Co promoted S-edges where constructed while keeping the M-edge unchanged.

2.2. Catalyst Preparation

Mo, NiMo, and CoMo catalysts were prepared by sequential incipient wetness impregnation of a $MgAl_2O_4$ spinel support supplied by Sasol as Al_2O_3·MgO precursor pellets (Puralox MG30 5x5, Z600134). This precursor was initially calcined for 3h at 1000 °C to obtain the $MgAl_2O_4$ structure

(verified by X-ray diffraction (XRD)). The calcined $MgAl_2O_4$ sample had a pore volume of 0.44 g_{water}/g (90 % of this volume was used for impregnation), and a pore volume determined by N_2-physisorption of 0.28 cm^3/g (see supplementary information Figure S.1 and Figure S.2 for physisorption isotherm and pore size distribution). The mean pore radius was 104.1 Å. The specific surface area, SSA, of the calcined $MgAl_2O_4$ was 60-62 m^2/g with little variation between the different batches calcined.

The support was crushed and sieved into a 300-600 µm fraction that was impregnated with an aqueous solution of $(NH_4)_6Mo_7O_{24}\cdot 4H_2O$ (Fluka ≥99.0 %). It was then aged (by stirring) for 1 h and dried at 110 °C overnight. For promoted catalysts, a second impregnation was performed similarly with $Co(NO_3)_2\cdot 6H_2O$ (Fluka ≥98 %) or $Ni(NO_3)_2\cdot 6H_2O$ (Sigma-Aldrich ≥97 %) followed by aging and drying at 110 °C overnight. Calcination was then performed in a flow of 2.5 NL/min technical air (20 % O_2 in N_2) by heating with a ramp of 5 °C/min to 500 °C and holding for 3 h. The catalysts were fractioned again (300-600 µm) before activity tests to remove any dust or agglomerates formed during the preparation. A catalyst with 14 wt% Ni was prepared as well to test the activity of supported NiS_x.

Catalyst activation was performed in-situ in the catalytic activity setup close to atmospheric pressure in a flow of 10-12 % H_2S created from dimethyl disulfide (DMDS, Sigma-Aldrich ≥99.0 %) in H_2; resulting in a total flow rate of ≈ 830 NmL/min. The temperature was ramped at 5 °C/min from 200 °C to 360 °C and held at 360 °C until unconverted DMDS started to build up in the outlet. The temperature and pressure was then increased to achieve reaction conditions.

Table 1 gives an overview of the prepared catalysts. The loading of Mo was targeted at a sub monolayer, which is <4 atoms/nm^2 for $MgAl_2O_4$ and thus similar to that of γ-Al_2O_3 [54]. This was done to ensure a high dispersion of small moderately active sulfide particles and thereby prevent the

formation of a highly active type II sulfide phase [13,55]. An estimated loading of 3.0-3.7 Mo atoms/nm^2 was achieved. The promoter loading was fixed at a M/Mo (M = Ni, Co) molar ratio of 0.3 to optimize the activity [13,56].

Table 1 Composition and properties of as-prepared calcined catalyst precursors (oxide phase).

Catalyst	Mo [wt%]	Ni [wt%]	Co [wt%]	Ni/Mo [molar]	Co/Mo [molar]	Mg [wt%]	Al [wt%]	Al/Mg [molar]	Mo load[a] Atoms/nm^2	BET SSA [m^2/g]
Mo#1	3.36	-	-	-	-	-	-	-	3.7	64
NiMo#1	2.83	0.58	-	0.34	-	-	-	-	3.0	97
NiMo#2	3.33	0.66	-	0.33	-	-	-	-	3.7	77
CoMo#1	3.28	-	0.59	-	0.29	-	-	-	3.5	73
CoMo#2	3.37	-	0.58	-	0.28	-	-	-	3.7	70
Ni#1	-	14.3	-	-	-	-	-	-	-	49
$MgAl_2O_4$ (support)	-	-	-	-	-	17.4	36.1	1.87[b]	-	60-62

a) Estimated loading in atoms Mo per nm^2 support surface area available (assuming presence of MoO_3, NiO, and CoO).
b) The slight excess of MgO was reported by Sasol and additionally verified by XRD.

2.3. Catalyst Characterization

Fresh and spent catalysts have been analyzed using various techniques. Inductively coupled plasma optical emission spectroscopy (ICP-OES) was used to determine the concentration of metals (Mo, Co, Ni, Fe, Si, Mg, and Al), and CS analysis by combustion and IR product detection (CO_2 and SO_2) was used to get the content of C and S (in spent catalysts). N_2-physisorption (BET and BJH) was performed at liquid nitrogen temperature, -196 °C, using a QuantaChrome Autosorb iQ_2 or Monosorb MS-21 gas sorption analyzer. The catalysts were outgassed for 2 h at 350 °C under vacuum, prior to N_2 physisorption in the p/p_0 range of 0.01-0.99. Transmission electron microscopy (TEM) was performed on an aberration corrected FEI Titan 80-300 operated at 300 kV.

Raman spectroscopy was performed using a Renishaw inVia Reflex Spectrometer System equipped with a frequency doubled Nd:YAG laser (532 nm, 100 mW). Data collection was typically performed in the 60-1300 cm^{-1} spectral range with a grating of 2400 lines/mm resolution. For each sample, an area of ca. 384 x 576 μm was scanned in a raster with 5400 points, which were averaged giving a single spectrum. To avoid sample heating, the laser was set to line shape at 10 % intensity

and the acquisition time was varied between 10 and 60 s per point. No dehydration was performed on the calcined catalysts prior to Raman spectroscopy; the molybdenum oxide precursor species were thus expected to be in their hydrated state [57,58].

2.4. Catalytic Activity Tests

Catalytic HDO activity tests were performed using a continuous fixed bed reactor setup with the simplified process diagram is shown in Figure 1. A detailed description of the setup excluding minor modifications can be found elsewhere [42].

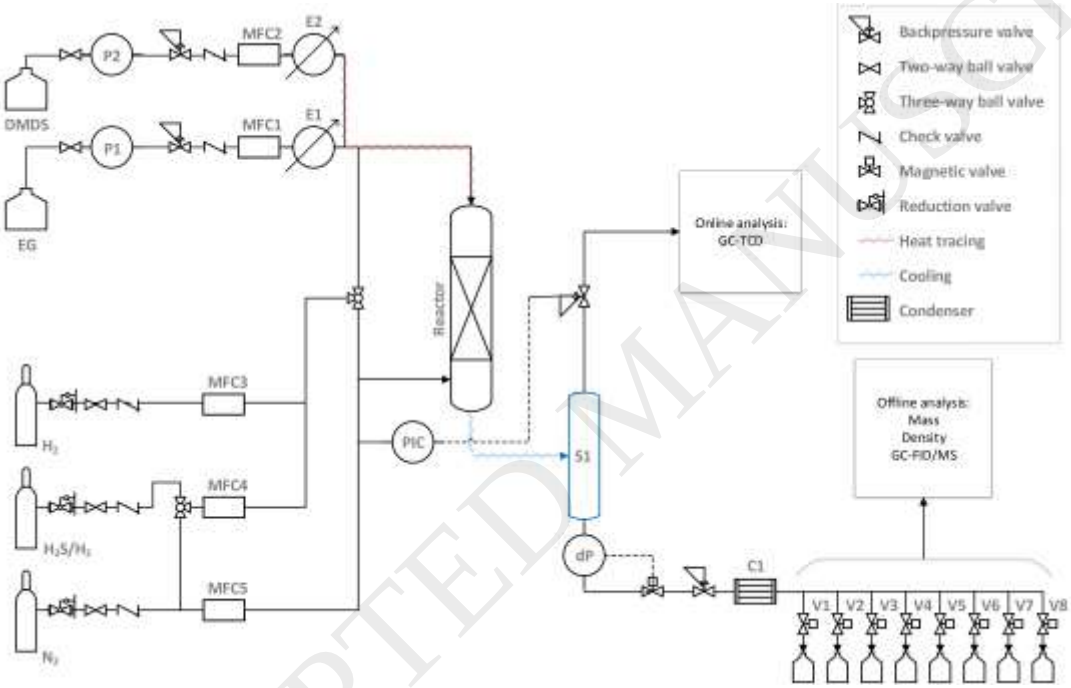

Figure 1 Simplified process diagram for the POC setup. MFC1-5: mass flow controllers, E1-2: evaporators, P1-2: pumps, S1: separator tube, PIC: pressure indicator and controller, dP: differential pressure cell, C1: condenser, V1-V8 manifold magnetic valves.

DMDS and ethylene glycol (EG, Sigma-Aldrich, ≥99.8 %) were pumped into the reactor top via two separate liquid feed lines (E1 heated to 80 °C). H_2 (≥99.9 %), N_2 (≥99.95 %), and 2 % H_2S/H_2 (≥99.5 %) were fed to the reactor via MFC3-5. The gas was fed at the bottom of the reactor where it flowed upward inside a pressure shell along the outer surface of the reactor until it was mixed with

the liquid feed in the top and entered the reactor tube in downflow. The reactor effluent was cooled to 10-15 °C and separated into gas and liquid in a separator tube, S1. The gas was analyzed online on a Shimadzu GC-2014 gas chromatograph (GC) with a thermal conductivity detector (TCD) and a 2 m 0.53 mm ID Shincarbon ST column (N_2, H_2, CO, CO_2, CH_4, C_2H_4, C_2H_6, C_3H_6, C_3H_8 were detected and analyzed). Liquid products were collected in a valve manifold (V1-V8) programmed for a 5 h collection frequency in separate sample bottles. The mass and density (using an Anton Paar DMA 4100 density meter) of liquid samples was measured to know the volumetric flow rate. The liquid composition was analyzed by GC-mass spectrometry (MS) using a Shimadzu 2010 GCMS-QP2010 Ultra fitted with an Equity®-5 30 m x 0.32 mm column with d_{film} 0.5 µm.

In activity tests, 0.5-1.5 g catalyst was diluted with 0.5-1.5 g SiC (150-250 µm) and fixed in a stainless steel reactor using steel wool to fixate the bed. Initial experiments using a quarts reactor tube, quarts wool, and glass beads for bed dilution, showed that all three glass components degraded upon exposure to ethylene glycol, H_2S, and H_2 under reaction conditions. Si was deposited on the catalysts, most likely on acid sites, which caused accelerated deactivation. In-situ activation was performed as described above. During reaction, ethylene glycol was fed to the reactor at a flow rate of ≈ 0.14 mL/min corresponding to a weight hourly space velocity (WHSV) of 6.2-19 g_{EG}/g_{cat}/h. Experiments were performed at 400 °C, 27 bar H_2, 550-2200 ppm H_2S, 40 barg total (balance N_2), total gas feed (H_2, N_2, H_2S) 1550 NmL/min, and 3-3.5 mol% ethylene glycol in the feed.

Experiments were terminated by stopping the ethylene glycol feed and changing from reaction gas to ≈ 500 NmL/min N_2 while reducing the pressure. When ambient pressure was reached, flushing with N_2 was continued at 400 °C to desorb condensed species from the catalyst pores. After 30 minutes flushing, the furnace was turned off to allow the system to cool to room temperature overnight while continuing the flow of N_2. Unloaded catalysts were separated from SiC and steel wool prior to analysis. No Soxhlet extraction was performed on spent catalysts prior to

characterization; thus, any condensed high-molecular weight products formed during reaction could be left in the catalyst pores.

2.5. Calculations

The conversion, X, of ethylene glycol was calculated based on the molar flow in, $F_{EG,feed}$, and out, $F_{EG,out}$, of the system:

$$X = \frac{F_{EG,feed} - F_{EG,out}}{F_{EG,feed}} \cdot 100\ \% \quad [1]$$

The carbon based yield of product i, Y_i, was calculated as:

$$Y_i = \frac{F_i \cdot \nu_{C,i}}{F_{EG,feed} \cdot 2} \cdot 100\ \% \quad [2]$$

F is molar flow rate and $\nu_{C,i}$ is the carbon number of compound i.

N_2 was used as internal standard in GC-TCD measurements so that the molar flow of H_2 and gaseous products could be determined as:

$$F_g = \frac{F_{N_2,feed}}{y_{N_2}} \quad [3]$$

$$F_{g,i} = y_i \cdot F_g \quad [4]$$

F_g is the total effluent molar gas flow based on the known molar feed flow of N_2, $F_{N2,feed}$, and the fraction of N_2, y_{N2}, determined by GC-TCD. $F_{g,i}$ is the resulting molar flow of compound i based on the composition (molar fraction, y_i) determined by GC-TCD.

The FID signal from the GC-MS/FID was calibrated for a range of compounds (methanol, ethanol, ethylene glycol, 1-propanol, ethyl acetate, and 1-butanol). A broader range of compounds were analyzed and quantified by using the effective carbon method [59]:

$$C_i = \frac{C_{ref} \cdot \nu_{Ceff,ref}}{A_{ref}} \cdot \frac{A_i}{\nu_{Ceff,i}} \quad [5]$$

The concentration of compound *i*, C_i, was calculated based on the area of the corresponding peak, A_i, on the effective carbon number of this compound, $\nu_{Ceff,i}$, and on the data from a reference compound (in this case ethanol). Data on effective carbon numbers can be found in the supplementary information, Table S.1. The molar flow rate of liquid phase compound *i*, $F_{l,i}$, was then found from the total liquid volumetric flow rate for the specific sample bottle, Q_l, which was determined based on the sample mass, m_l, sample density, ρ_l, and sampling time, *t*, for the specific sample bottle analyzed:

$$F_{l,i} = C_i \cdot Q_l \quad [6]$$

$$Q_l = \frac{m_l}{\rho_l \cdot t} \quad [7]$$

The carbon mass balance was calculated based on the flow of carbon into and out of the system, where *n* denotes the total number of compounds analyzed in the outlet (gas and liquid) including unconverted ethylene glycol:

$$C_{Balance} = \frac{\sum_i^n F_i \cdot \nu_{C,i}}{F_{EG,feed} \cdot 2} \cdot 100\ \% \quad [8]$$

Space time yields, STY, were calculated for C_1, C_2, and C_3 gas products to compare the catalyst productivity based on the mass of catalyst, m_{cat}, and the molar carbon based product of the compound of interest:

$$STY_i = \frac{F_i \cdot \nu_{C,i}}{m_{cat}} \quad [9]$$

The ratio of fully deoxygenated products (ethane and ethylene) to C_1 gas products (CO, CO_2, and CH_4) was used to assess the degree of HDO compared to cracking:

$$\frac{C_2}{C_1} = \frac{Y_{C_2H_6} + Y_{C_2H_4}}{Y_{CO} + Y_{CO_2} + Y_{CH_4}} \quad [10]$$

2.6. In-situ X-ray Absorption Spectroscopy (XAS):

XANES and EXAFS spectra were collected at the SuperXAS beamline at SLS (2.4 GeV storage ring, 400 mA ring current) [60]. Measurements were conducted at the Ni K- (8.333 keV), Co K- (7.709 keV), and Mo K-edge (20 keV) of the prepared Mo, NiMo, and CoMo catalysts. The catalysts were loaded into a 1 or 1.5 mm microreactor, which was based on quartz capillaries and was heated by a gas blower [61,62]. The reactor was connected to a H_2S gas feed line and could be switched between 1000 ppm or 10 % H_2S/H_2, and to a H_2 feed line, which could be sent through a water saturator or directly to the reactor. The total flow through the capillary reactor was 40-43 NmL/min. The exhaust was sent through a H_2S absorber (3.5 mol/L NaOH solution) into the exhaust system of the beamline. A N_2 line was installed for flushing. Quick EXAFS (QEXAFS) spectra were recorded in transmission mode with frequency of 10 Hz using ionization chambers as detectors and using an excentre disk to continuously move the monochromators in an oscillating manner allowing for fast measurements [60]. Reference spectra were recorded for MoS_2, MoO_3, MoO_2, $(NH_4)_6Mo_7O_{24}{\cdot}4H_2O$, $MoO_3{\cdot}H_2O$, CoS, CoO, Co_2O_3, Co_3O_4, Ni_3S_2, and NiO (pressed as BN pellets as received).

The catalysts were first dehydrated in a flow of N_2 while heating at 10 °C/min from room temperature (RT) to 200 °C. Sulfidation was then performed by heating until 400 °C at 5 °C/min in a flow of 10 % H_2S/H_2 and holding at 400 °C for 1 h. Sulfidation was followed by exposure of the catalyst to increasing ratios of H_2O/H_2S in H_2 with a constant total flow rate of 43 NmL/min at 400-450 °C. The holding time at each H_2O/H_2S ratio was typically 30 minutes. A schematic illustration of the experimental procedure employed for in-situ XAS measurements is given in the supplementary information, Figure S.3.

EXAFS spectra were analyzed by using the software package IFEFFIT interfaces, i.e., Athena and Artemis [63]. Athena was first employed to process the raw data, which included removal of smooth background from the measured absorption coefficient, normalization of the X-ray absorption coefficient, and Fourier transform of the resulting spectra from *k*-space to R-space. Artemis was used for fitting a theoretical model to the experimental data in the R-space to obtain the structural parameters. The model included amplitude reduction factor (S_0^2), coordination number (CN), Debye-Waller factor (σ^2), energy shift for each path (ΔE_0), and change in the path length (ΔR), where R is the bond length. Ab initio XANES calculations were performed using the FEFF9 code [64,65] as described in the S.I.

3. Results and Discussion

3.1. DFT Phase Diagrams

Unpromoted MoS_2 can exhibit a triangular crystal structure exposing only one type of edge, or a hexagonal (truncated triangle) structure depending on the H_2S/H_2 ratio [66]. Promoted MoS_2 exhibits a hexagonal structure with exposure of pure M- and metal doped S-edges [67–70]. For NiMoS, a less systematic distorted hexagonal structure has also been reported [68]. Figure 2 shows the calculated phase diagrams for unpromoted MoS_2 (M-edge), Ni-MoS_2 (S-edge), and Co-MoS_2 (S-edge) at varying H_2O/H_2S partial pressures and 400 °C. Due to the inherent uncertainty associated with generalized gradient approximation (GGA) DFT, it must be noted that the phase diagrams are representative of the trends between the different materials, but do not reflect precise numbers. Thus, the partial pressures of water and H_2S mentioned in the remainder of this section serve the purpose of distinguishing the different edge structures obtained from DFT to clarify the general trends observed in Figure 2 at varying partial pressures of H_2S and H_2O.

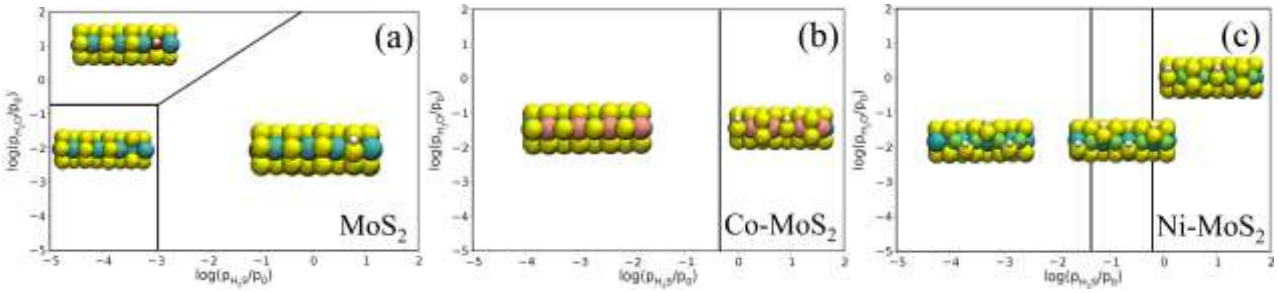

Figure 2 Phase diagrams as funtion of the partial pressure of water and H_2S for (a) the unpromoted MoS_2 M-edge, and the promoted S-edges of (b) Co-MoS_2, and (c) Ni-MoS_2 as obtained from DFT calculations. Yellow = S, blue = Mo, pink = Co, green = Ni, red = O, white = H. Total pressure 40 bar, 27 bar H_2, 400 °C, p_0 = 1 bar.

The MoS_2 edge has a single S-vacancy and exhibits a $Mo_{1.00}S_{0.75}$ structure in the range of $\log(p_{H2O}/p_0) < -0.7$ and $\log(p_{H2S}/p_0) < -3$ corresponding to ≈ 0.3-5000 ppm H_2O and ≈ 0.3-30 ppm H_2S (see Figure 2a). An OH group adsorbs on the vacancy site if the H_2O pressure is increased further, resulting in a $Mo_{1.00}S_{0.75}(OH)_{0.25}$ edge structure. If instead the H_2S concentration is increased above 30 ppm, an SH group adsorbs on the vacancy (H_2O concentration <5000 ppm) and the edge structure becomes $Mo_{1.00}S_{1.00}H_{0.25}$. In the concentration range of >5000ppm H_2O and 30 ppm to 1.5 % H_2S, the H_2O/H_2S ratio should be kept below ≈ 150 to avoid an S-O exchange at the surface. At a H_2S concentration >1.5 %, no S-O exchange is observed no-matter the H_2O pressure. These results indicate that a certain concentration of H_2S should be fed during HDO to avoid oxidation of unpromoted MoS_2 in line with results from other theoretical work [41].

The Co promoted MoS_2 does not exhibit any vacancy formation or S-O exchange in the investigated H_2O/H_2S ranges, which indicates that Co stabilizes the active edge against oxidation (see Figure 2b). Below $\log(p_{H2S}/p_0) = -0.3$, corresponding to ≈ 1 % H_2S, the S-edge is fully decorated with S (edge structure $Co_{1.00}S_{1.00}$), and if the H_2S pressure is increased, two additional S atoms and two H atoms are adsorbed on the surface giving the edge structure $Co_{1.00}S_{1.50}H_{0.50}$. This indicates that the $Co_{1.00}S_{1.00}$ structure has CUS, which could act as active sites for oxygenate adsorption and deoxygenation [46].

Ni promotion also stabilizes the edge; no S-O exchange is observed at the investigated conditions (see Figure 2c). Three stable phases were obtained with structures that are less ordered compared to the Co promoted analogue; $Ni_{1.00}S_{0.75}H_{0.75}$, $Ni_{1.00}S_{1.00}H_{1.00}$, and $Ni_{1.00}S_{1.50}H_{0.50}$ at low, intermediate, and high H_2S concentration, respectively. H atoms are adsorbed on the surface in the entire H_2S partial pressure range. A single sulfur vacancy is present below ≈ 1000 ppm H_2S ($\log(p_{H2S}/p_0) = -1.35$). At ≈ 1000 ppm to 1.5 % H_2S ($\log(p_{H2S}/p_0) = [-1.35;-0.21]$), the edge is fully decorated with S exhibiting a $Ni_{1.00}S_{1.00}H_{1.00}$ structure. At higher concentrations, more S is adsorbed indicating presence of CUS at <1.5 % H_2S.

3.2. Conversion of Ethylene Glycol over Promoted and Unpromoted $MoS_2/MgAl_2O_4$

Based on the results from the catalytic activity tests, HDO of ethylene glycol is proposed to follow a reaction mechanism involving consecutive dehydration and hydrogenation steps (Figure 3):

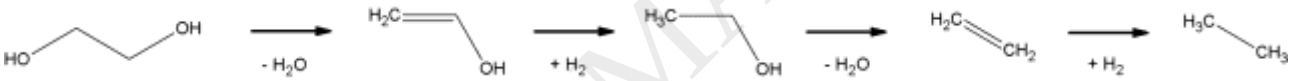

Figure 3 Proposed reaction mechanism for HDO of ethylene glycol via consecutive dehydration and hydrogenation reactions.

3.2.1. Overall Activity

The results from the activity tests of MoS_2 based catalysts are shown in Figure 4 (conversion, STY, and C_2/C_1) and Figure 5 (yields of ethane, ethylene, and ethanol). All gas product yields can be found in the supplementary information, Figure S.9.The conversion of ethylene glycol was in the range ≈ 50-100 % for the prepared catalysts, and the selectivity towards HDO in terms of the C_2/C_1 ratio followed the trend MoS_2 > Ni-MoS_2 ≈ Co-MoS_2 > NiS_x (see Figure 4).

A blank experiment (steel reactor packed with steel wool and SiC) showed negligible HDO activity; ethylene was the main gaseous product formed with a yield <0.7 %. In all experiments performed using MoS_2 based catalysts, the yield of ethane and ethylene, respectively, was in the range of ≈ 5-

45 % depending on the catalyst and level of deactivation. The detected yield of ethanol was 4.5-18 % and accounted for the majority, ≈ 35-55 %, of carbon in the liquid products formed. Cracking reactions also occurred, resulting in the formation of CH_4, CO, and CO_2; the latter possibly through the water gas shift reaction. C-C bond formation also occurred forming small amounts of C_{3+} gas and liquid species, e.g. propane, propylene, 1-propanol, butane, and 1-butanol.

Coupling reactions forming e.g. 2-methyl-1,3-dioxolane and 4-polyethyleneglycol were also observed and ascribed to the support acidity, which is known to catalyze coupling reactions such as transalkylation, polymerization, and coking [27,71,72]. The conversion of ethylene glycol over the pure $MgAl_2O_4$ support (1.0 g) produced an insignificant total gas carbon yield of ≤ 2 % (C_1, C_2, and no C_3) and a more significant yield of 2-methyl-1,3-dioxolane (≤5.6 %), diethylene glycol (≤4.5 %), and ethanol (≤4.4 %) over 52 h on stream at a conversion of 13-41 %. Partly deoxygenated and reactive intermediates, such as ethyl or ethoxy groups can readily undergo polymerization if they are not stabilized by hydrogenation into ethane. Ethylene and propylene are known to be strong coke precursors [73].

Ni-sulfides have shown moderate activity in HDO [74]. The tested Ni catalyst, however, showed poor HDO selectivity at 55-65 % conversion with a C_2/C_1 ratio ≈ 1 at 550 ppm H_2S and low STYs <0.3 mmol/g_{cat}/min (see Figure 4a). The C_2/C_1 ratio could be increased to ≈ 1.5 at 2200 ppm H_2S; mainly by increasing the yield of ethylene, while the yield of ethane remained <1.5 % and the C_2 STY remained low (see Figure 5a).

The presence of promotor and the feed concentration of H_2S influenced the activity and stability of the Mo, NiMo, and CoMo catalysts as discussed in section 3.2.3. During the first ≈ 50-70 h of time on stream (TOS), the feed contained 550 ppm H_2S. Then, the H_2S concentration was increased by a factor of four to 2200 ppm. For the NiMo catalyst (see Figure 4c and Figure 5c), a subsequent

decrease of H_2S down to 1900 ppm was performed from ≈ 140-160 h on stream, followed by a stepwise shutoff of H_2S. For the CoMo catalyst, (see Figure 4d and Figure 5d), an issue with the ethylene glycol feed arose at TOS) ≈ 80-90 h. In that period, the feed consisted of reaction gas (N_2, H_2, H_2S) without ethylene glycol.

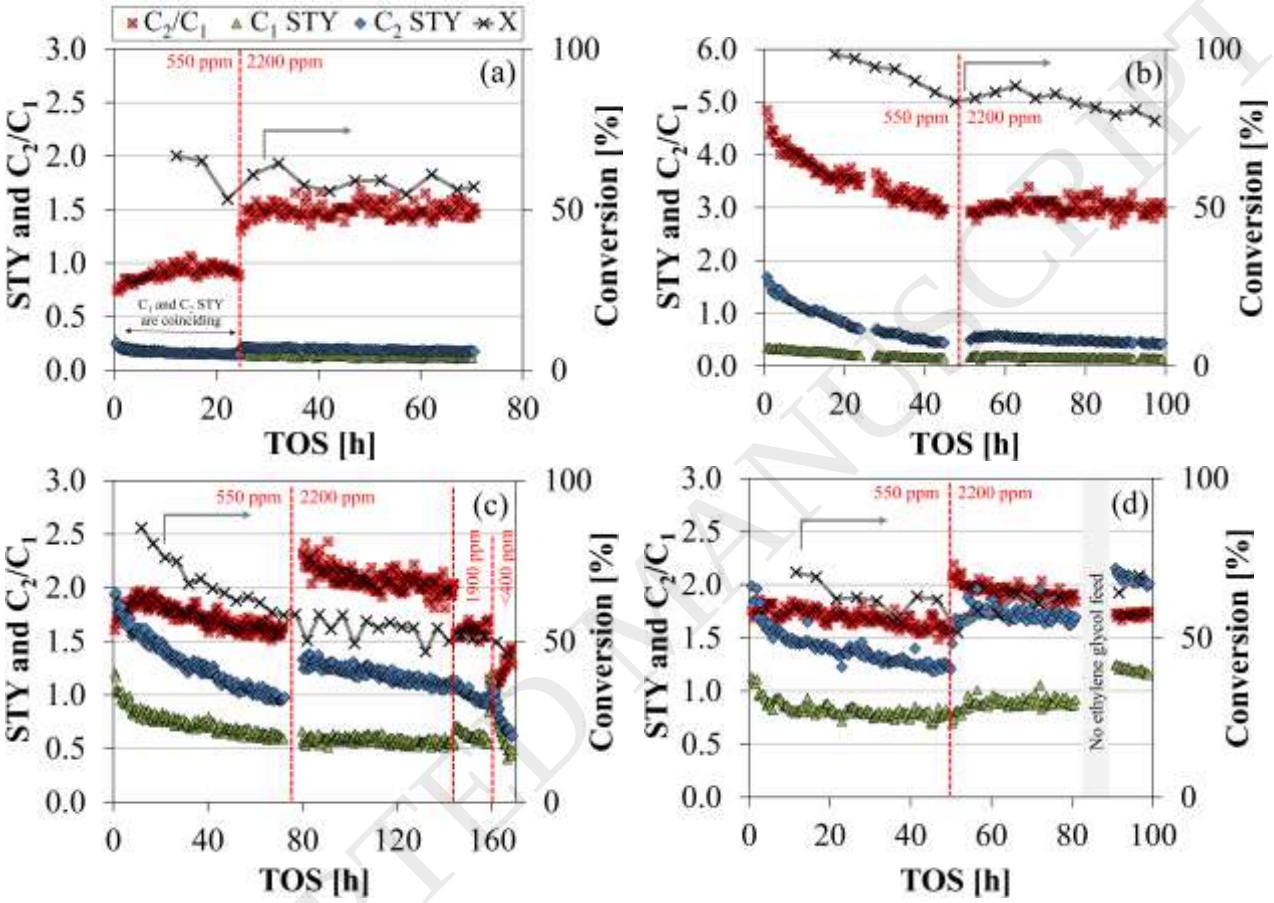

Figure 4 STY [mmol/g_{cat}/min], C_2/C_1 ratio [-], and conversion for ethylene glycol conversion at 400 °C, 27 bar H_2, 550-2200 ppm H_2S (noted in figures), 40 barg total (balance N_2), and 3-3.5 mol% ethylene glycol in the feed for (a) Ni#1(1.5g), (b) Mo#1 (1.5g), (c) NiMo#1 (0.5g), and (d) CoMo#1 (0.5g) in Table 1. Cooling on separator tube S1 was not installed in experiments (c) and (d).

3.2.2. Carbon Mass Balance

The carbon mass balance could not be fully closed for the presented experiments; the balance closure at TOS >20h was 69-83 % for NiS_x (Figure 4a), 63-76 % for Mo (Figure 4b), 72-84 % for NiMo (Figure 4c), and 73-91% for CoMo (Figure 4d), and. The lack of closure in the mass balance was ascribed to the presence of mainly non-condensed oxygenate compounds in the gas phase, which were not detected or quantified. Based on offline GC-FID and GC-TCD analysis of gas

samples from experiments similar to those presented in this work, it was found that the product gas contained non-condensed hydrocarbons (C_{4-6} isomers) and oxygenates (ethanol, acetaldehyde, methanol, 2-propanone, 1- and 2-propanol, 2-butanone, and 2-pentanone), which could not be detected by the online GC analysis. These compounds were present in concentrations, which could account for the majority of the missing carbon. As a consequence, the yield of ethanol (Figure 5) can be assumed to be higher than reported here. In order to improve the carbon balance, it can be considered to perform online analysis of the oxygenates and C_{4+} hydrocarbons present in the gas phase, and to improve cooling further in the liquid product collection and storage.

In an experiment using 4g NiMo, 100 % conversion into gas and pure water was obtained, and the mass balance could be closed within 87-96 % (no cooling of S1). Also, a >20 h empty tube test conducted at 400 °C and 40 barg, feeding 500 NmL/min N_2 and 0.14 mL/min ethylene glycol had an average carbon balance of 95 % (no cooling of S1). Elemental carbon analysis of four liquid samples from the Mo test (Figure 4b, 68-83 h) using a Eurovector EA3000 CHNS analyzer was used to confirm that the carbon content determined by GC-MS was precise within a deviation of <10 %. Thus, the gas product results (yields, STY, and C_2/C_1) and the conversion (based on unconverted ethylene glycol) are not affected by the discrepancy in the carbon mass balance.

3.2.3. Role of Promotion and H_2S in the C_2/C_1 Selectivity and Stability

Unpromoted Mo showed a very favorable selectivity towards HDO products compared to the promoted catalysts. The ratio of C_2/C_1 was approximately ≥3 for the entire run (see Figure 4b), while it was <2.5 for the promoted catalysts (see Figure 4c-d). The mass based productivity was, however, lower for the unpromoted catalyst, which initially had a C_2 STY was 1.7 mmol/g_{cat}/min, while it was 1.9-2.0 mmol/g_{cat}/min for the promoted catalysts. Furthermore, the unpromoted catalyst was subject to significant deactivation. After 40 h on stream, the C_2 STY was 0.5 mmol/g_{cat}/min and had thereby decreased by 70 %. In the same period of time, the C_2/C_1 ratio dropped by 30 % from

4.8 to 3.3, showing a decrease in HDO selectivity. In comparison, the promoted catalysts only deactivated with 35 % in terms of the C_2 STY in the same period of time reaching 1.2 mmol/g_{cat}/min at 40 h. The initial decrease in the C_2/C_1 ratio was similar for NiMo and CoMo reaching 1.6 at 40 h. Promotion with Ni or Co was therefore seen to enhance the activity of the catalyst, which is in agreement with other studies on the role of promotion in HDO and HDS over MoS_2 based catalysts [33,41,43,68,75,76]. The selectivity to HDO products was, however, higher for the unpromoted catalyst.

As the H_2S concentration was increased from 550 to 2200 ppm at TOS ≈ 50 h for the unpromoted catalyst, a slight stabilizing effect was obtained, but the activity remained low (see Figure 4b). For both NiMo and CoMo, the C_2 STY increased when the H_2S concentration was increased to 2200 ppm and a stabilized activity was obtained. For NiMo (see Figure 4c), the C_2 STY increased from 0.98 to 1.3 mmol/g_{cat}/min (at TOS ≈ 75-80 h) resulting in a C_2/C_1 improvement from 1.6 to 2.3. For CoMo (see Figure 4d), the C_2 STY increased from 1.2 to 1.7 mmol/g_{cat}/min (at TOS ≈ 50 h) giving a C_2/C_1 increase from 1.6 to 2.0, since there was also a slight increase in the C_1 STY. The conversion of ethylene glycol did not increase, as the H_2S concentration was changed during each experiment (see Figure 4), but a slight stabilization of the conversion occurred as the H_2S concentration was increased from 550 to 2200 ppm.

For the NiMo catalyst, it was seen that with a slightly lower H_2S concentration of 1900 ppm (TOS ≈ 140-160 h), deactivation occurred at a faster rate than at 2200 ppm H_2S, and the selectivity towards cracking products increased (see Figure 4c). A further decrease to <400 ppm H_2S caused severe deactivation. It can be concluded that a feed of H_2S is necessary to keep the catalyst active and that this concentration should be in the order of 2200 ppm at the applied conditions to ensure a higher selectivity towards HDO and a stable activity.

As the ethylene glycol flow was reapplied after feed issues at TOS ≈ 80-90 h (see Figure 4d) during the CoMo test, the catalyst was more active with a slightly higher conversion (65-70 % at 92-97 h compared to 61-63 % at 72-77 h) and a higher yield of both cracking and HDO products. The activity in terms of yields of ethane (see Figure 5d) and some C_1 gasses (see also supplementary information, Figure S.9) increased to a level above the initial activity after the period without ethylene glycol in the feed. Based on the DFT findings (see Figure 2b), it could be speculated that before ethylene glycol is shut off, several CUS were occupied by ethylene glycol and reaction intermediates, while the ethylene glycol free period at the high concentration of H_2S might have either released CUS, increased the concentration of SH at the surface, or both, resulting in a higher HDO activity.

3.3. Role of H_2S in Primary Alcohol HDO

The yield of ethane and ethylene (see Figure 5) reflected the trends observed in the STYs and C_2/C_1 ratio (see Figure 4). The Ni catalyst had a poor hydrogenation activity, resulting in a 3-5 times higher yield of ethylene compared to ethane at TOS > 5h (see Figure 5a).

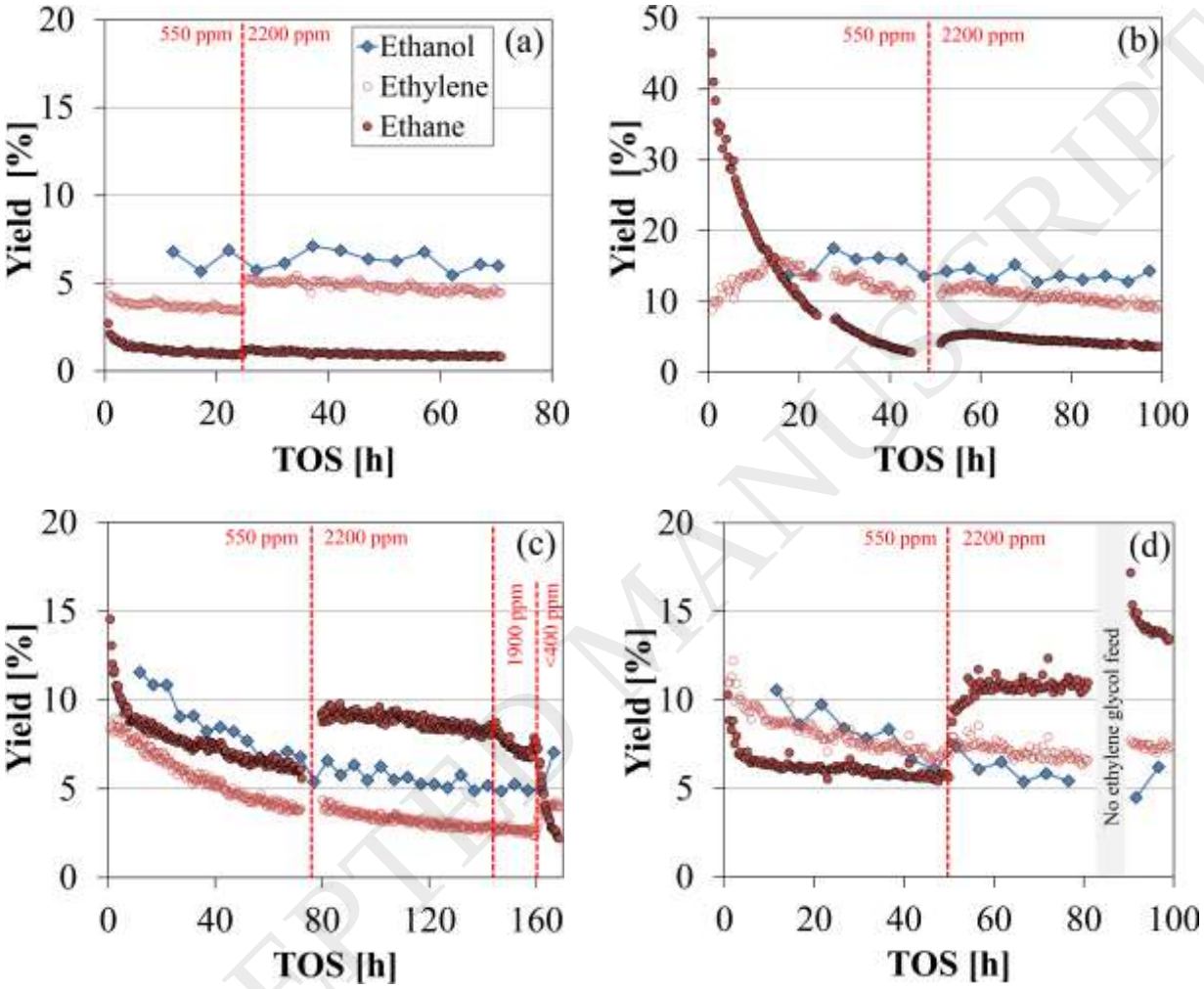

Figure 5 Carbon based yields for ethylene glycol conversion at 400 °C, 27 bar H_2, 550-2200 ppm H_2S (noted in figures), 40 barg total (balance N_2), and 3-3.5 mol% ethylene glycol in the feed for (a) Ni#1(1.5g), (b) Mo#1 (1.5g), (c) NiMo#1 (0.5g), and (d) CoMo#1 (0.5g) in Table 1. Cooling on separator tube S1 was not installed in experiments (c) and (d).

For the unpromoted Mo catalyst (see Figure 5b), there was an initial fast change in the relative proportions of the yields of ethane and ethylene, caused by deactivation of the hydrogenation activity. The initial ethane yield was 45 % compared to an ethylene yield of 9 %. At 15 h on stream,

the ethane yield had dropped and the ethylene yield had increased, both reaching ≈ 15 %. After this point in time, the ethane yield continued to decrease, and the ethylene yield also decreased, however, at a slower rate. The lower hydrogenation activity of the unpromoted catalyst compared to the promoted catalysts (see Figure 5b-d), was ascribed to the ability of Ni and Co promotion to facilitate adsorption of H at the surface as evidenced by DFT calculations (see Figure 2), thereby providing better hydrogenation activity [33,68,75,76].

For NiMo (see Figure 5c), the ethane yield was higher than the ethylene yield during the entire TOS, as long as H_2S was added to the feed, which could be explained by the high concentration of H adsorbed at the S-edge (see Figure 2c). As the H_2S concentration was increased from 500 to 2200 ppm, the ethane yield increased from ≈ 6 to 9 %, while the ethylene yield overall remained unchanged. This increase in ethane yield could possibly be explained by the change of a $Ni_{1.00}S_{0.75}H_{0.75}$ S-edge structure to $Ni_{1.00}S_{1.00}H_{1.00}$ providing more hydrogen in terms of additional SH groups (see Figure 2c).

For CoMo (see Figure 5d), the yield of ethylene was initially higher than that of ethane, until the H_2S concentration was increased from 500 to 2200 ppm, causing the yield of ethane to increase above that of ethylene (from ≈ 6 to 10 %), which remained rather unchanged (at 7-8 %). These observations could be explained by the change in the S-edge structure from $Co_{1.00}S_{1.00}$ to $Co_{1.00}S_{1.50}H_{0.50}$, which provides more hydrogen through SH groups (see Figure 2b).

Since only ethane and not ethylene seemed to be affected by the change in H_2S, this indicates that the hydrogenation of ethylene to ethane in reaction in Figure 3 is very fast, and that an increased H_2S concentration of 2200 ppm increased both the deoxygenation and hydrogenation activity.

Mortensen [42] saw that even though an increase from 283 to 8172 ppm H_2S (at 280 °C and 100 bar) inhibited the conversion of phenol over a Ni-MoS_2/ZrO_2 catalyst, the conversion of 1-octanol

(used as solvent), was increased from 50-75 % to 85-100 % during the 100 h TOS test. In line with this observation, Şenol et al. [29,45] reported that while H_2S had an inhibiting effect on the HDO of aromatic oxygenates (due to competitive adsorption of H_2S), HDO of aliphatic oxygenates was promoted by increasing H_2S owing to their different reaction mechanisms that depend on acid-catalyzed reactions; e.g. dehydration and hydrogenation. These reactions have been proposed to be governed by the presence of nucleophilic SH groups present at the catalyst surface, which have been suggested to supply hydrogen and provide Brønsted acidity for HDO and HDS reactions [45,47,48,77]. Şenol et al. [29] also reported that increasing the H_2S concentration increased the activity and stability of $NiMo/Al_2O_3$ and $CoMo/Al_2O_3$ catalysts in the HDO of methyl heptanoate at 250 °C and 15 bar.

Based on the findings in this work, it is therefore proposed that the role of H_2S in the conversion of ethylene glycol is to increase and maintain a high concentration of SH groups at the catalyst surface, which correspondingly aid catalysis of the consecutive dehydration/hydrogenation reactions of ethylene glycol to ethylene and ethane (see Figure 3). This is supported by the DFT calculations, which showed that the concentration of adsorbed S and H generally increased with increasing H_2S pressure (see Figure 2).

3.3.1. Reproducibility of Stabilizing Effect of H_2S

Generally, fast deactivation was seen in the beginning of the catalytic activity tests (see Figure 4 and Figure 5). Thus, two additional short terms experiments were performed to investigate whether the observed stabilizing effect of H_2S had also been affected by general stabilization of the catalyst activity over time. Two fresh loads of CoMo (CoMo#2 with comparable composition to CoMo#1, see Table 1) were tested for ethylene glycol conversion with a H_2S feed concentration of 550 and 2200 ppm, respectively (see Figure 6). The TOS of 8 h was too short to collect liquid products for

calculation of conversion. Instead, the total carbon yield of C_{1-3} gas products indicates the minimum conversion level.

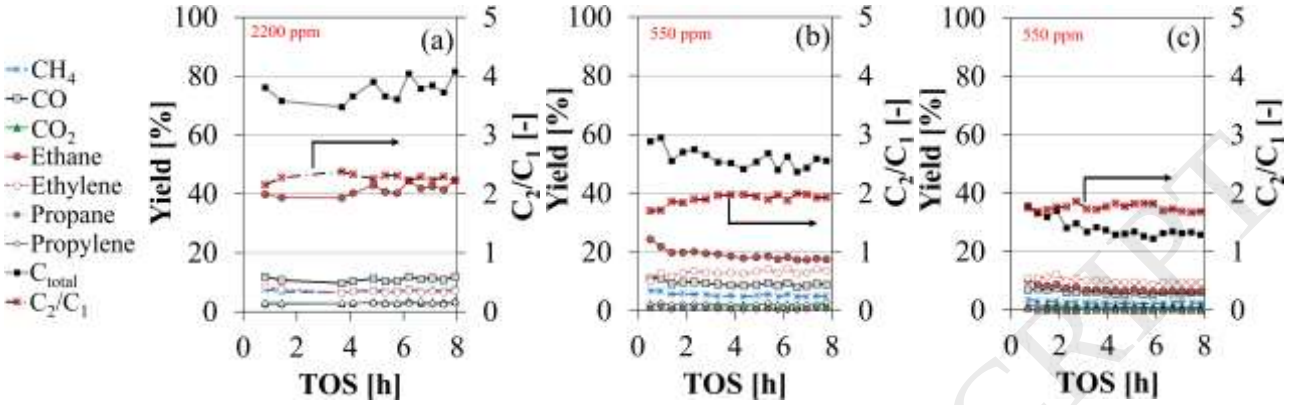

Figure 6 Carbon based yields for ethylene glycol conversion at 400 °C, 27bar H_2, 550-2200 ppm H_2S (noted in figures), 40 barg total (balance N_2), and 3-3.5 mol% ethylene glycol in the feed with 0.5g catalyst for (a) CoMo#2 at 2200 ppm H_2S, (b) CoMo#2 at 550 ppm H_2S, and (c) CoMo#1 at 550 ppm H_2S (same experiment as presented in Figure 4d and Figure 5d). For catalyst composition, see Table 1. C_{total} denotes total carbon yield in detected gas products.

An initial feed concentration of 2200 ppm H_2S (see Figure 6a) resulted both in a higher activity (total carbon gas yield >70 %) and better HDO selectivity with $C_2/C_1 \approx 2.3$ compared to the lower feed concentration of 550 ppm H_2S, where the total carbon gas yield was ≈ 45-60 % and the C_2/C_1 ratio was 1.7-2.0 (see Figure 6b). For 2200 ppm H_2S, there was a stable (actually slightly increasing) activity over time, while for 550 ppm H_2S deactivation occurred over time confirming the stabilizing effect of H_2S.

There was some deviation between the activity observed during the first 8 h on stream at 550 ppm H_2S with CoMo#1 (see Figure 6c) and CoMo#2 (see Figure 6b), which is essentially an attempted reproduction. A higher activity was obtained for CoMo#2, namely in terms of the ethane yield, but as it can be seen from the long TOS activity tests (see Figure 5), the initial 10 h period on stream is subject to significant activity changes, and it is recommended to run experiments for long TOS to decouple the initial activity from the long term performance. Also, it should be noted that two different catalyst batches were used for the experiments in Figure 6a-b (CoMo#2) and c (CoMo#1).

As discussed later (see section 3.5.3), it is possible that the lower activity obtained in CoMo#1 was caused by formation of Co_9S_8.

Reproducibility was obtained for the NiMo#1 catalyst (see supplementary information, Figure S.10), though it was seen that especially the ethane yield, temperature, and conversion were subject to smaller variations. These parameters are correlated, and it is believed that the specific morphology and dispersion of the active phase obtained through the sulfidation could vary slightly and consequently affect the ethane production and thereby also the conversion and temperature. This indicated different sulfidation behavior of the loaded catalysts (even from the same batch), indicating the complex nature of sulfide catalysts [13].

3.4. Spent Catalyst Composition

The composition of spent catalysts is given in Table 2. The deposited carbon (3.4-12 wt%) is approximately linearly correlated with the TOS (see supplementary information, Figure S.11) indicating that carbon deposition is a major source of deactivation. This was further evidenced as resulfidation of both spent Mo and NiMo catalysts (tested for ethylene glycol conversion at slightly different conditions), could only reactivate the catalyst for a short period of time. The activity of the reactivated catalysts was lower than the initial activity and the catalysts were subject to rapid deactivation; within <4 h on stream after reactivation, the activity had dropped to the same level as was achieved prior to the resulfidation.

The S/Mo ratio followed the trend NiMo#1 > CoMo#1 > Mo#1 > CoMo#2 (see Table 2). Ni promotion has been shown to facilitate faster sulfidation of MoO_x into MoS_2 (see Figure 11 in section 3.5.2), which might explain the high content of sulfur in the spent NiMo catalyst. The S/Mo ratio of ≈ 2 for CoMo#1 indicated that a stoichiometric MoS_2 phase was present in the spent catalyst, but for CoMo#2, including a fresh sulfided sample, this ratio was 1.52-1.70 indicating the complex nature of sulfides and the difficulties in obtaining identical sulfide phases in different

experiments. The elemental composition should however be interpreted with caution and more advanced in-situ characterization tools are needed to determine the phases present (see section 3.5). In this case, the elemental composition does not reveal if there were any presence of segregated Ni or Co sulfides, or if any C or S was present as condensed species in the catalyst pores.

The M/Mo (M = Ni, Co) ratio of the spent catalysts was slightly lower than in the fresh catalysts, but it remained approximately constant at 0.3 indicating that Mo, Ni, and Co are stable against volatilization; potentially induced by e.g. H_2O and CO.

Table 2 Composition and properties of spent catalysts (activity tests presented in Figure 4, Figure 5, and Figure 6) including TOS and H_2S feed concentrations used.

Catalyst	**TOS [h]**	**H_2S [ppm]**	**Mo [wt%]**	**Ni [wt%]**	**Ni/Mo [molar]**	**Co [wt%]**	**Co/Mo [molar]**	**Si [wt%]**	**Fe [wt%]**	**S [wt%]**	**C [wt%]**	**S/Mo [molar]**
Mo#1	99	500, 2200	2.48	-	-	-	-	0.05	0.05	1.47	10.4	1.78
NiMo#1	169	500, 2200, 1900, <400	2.52	0.44	0.28	-	-	-	0.06	1.90	12.0	2.25
CoMo#1	90	500, 2200	2.54	-	-	0.41	0.26	0.04	0.04	1.72	10.8	2.02
CoMo#2a	8	2200	3.31	-	-	0.52	0.26	0.05	<0.02	1.76	3.61	1.56
CoMo#2b	8	500	3.15	-	-	0.49	0.25	0.03	<0.02	1.60	3.44	1.52
CoMo#2fresh[a]	0	-	3.11	-	-	0.49	0.25	0.02	0.02	1.76	2.83	1.70
Ni#1	71	500, 2200	-	12.0	-	-	-	0.04	0.05	3.54	6.82	0.54 (S/Ni)

a) Sulfided and subsequently exposed to the same procedure of increasing temperature and pressure as applied in experiments. At the point in time, where ethylene glycol would normally be added, flushing and cooling was performed according to the procedure applied for experiment shutdown.

3.5. Characterization of Active Phases

3.5.1. Oxide Phase

The calcined catalyst precursors (see Table 1) were analyzed with Raman spectroscopy to assess the dispersion of Mo, NiMo, and CoMo phases (see Figure 7). The identification of the various phases

present was supported by curve fitting analyses (see supplementary information, Figure S.12 and Table S.2).

Broad main signals around 910 and 895 cm^{-1} were found indicating a small crystallite size of tetrahedrally coordinated MoO_4^{2-} species [57,78]. The bands can be assigned to symmetric and asymmetric stretching modes, while broad bands around 315 cm^{-1} are caused by the bending modes of terminal Mo=O [57]. The lack of broad bands at 200-230 cm^{-1} (Mo-O-Mo vibration) and 943-965 cm^{-1} further suggests that the tetrahedral entities were isolated and not present as polymolybdates, which is in agreement with the low catalyst loading that was applied [57,58,78]. For NiMo#1, the main band is slightly shifted to lower wavenumbers, which may represent a lower bond order (higher coordination) or a longer atomic distance of MoO_4^{2-} species. The Raman bands at 406, 670, and 769 cm^{-1} refer to the E_g, F_{2g}, and A_{1g} modes of the support material, $MgAl_2O_4$ [79] and were found for all samples. An additional Raman band at 555 cm^{-1} was found for NiMo#1 and corresponds to supported and dispersed NiO [80]. Similarly, a Raman band at 593 cm^{-1} can be attributed to supported CoO for CoMo#1 [80].

Bulk $NiMoO_4$, $CoMoO_4$, and MoO_3 is unwanted, as crystallites of these phases do not convert into the active NiMoS and CoMoS phases during sulfidation [31]. No sharp Raman bands of crystalline $NiMoO_4$ (≈ 912 and 962 cm^{-1}) or $CoMoO_4$ (≈ 936 (α-$CoMoO_4$ or 935 and 946 cm^{-1} (β-$CoMoO_4$)) [81,82] were observed. For CoMo#1, no bulk Co_3O_4, CoO, or $CoAl_2O_4$ was found (≈ 480, 520, 620, and 690 cm^{-1}) [83,84] and similarly, the lack of a broad peak around 525 cm^{-1} for NiMo#1 indicated that no bulk NiO was present in this catalyst precursor [85]. In general, the presence of bulk MoO_3 (667, 820, and 992 cm^{-1}) [57] could be ruled out for all catalyst precursors. Supported MoO_x may show Raman shifts at higher wavenumbers than 992 cm^{-1} [86]. Nevertheless, this may not explain the observed Raman bands between 1045-1090 cm^{-1} (Figure 7). Minor Si impurities with a

characteristic Raman shift at 521 cm^{-1} were assigned to potential impurities in the support or in the Mo precursor used for the preparation.

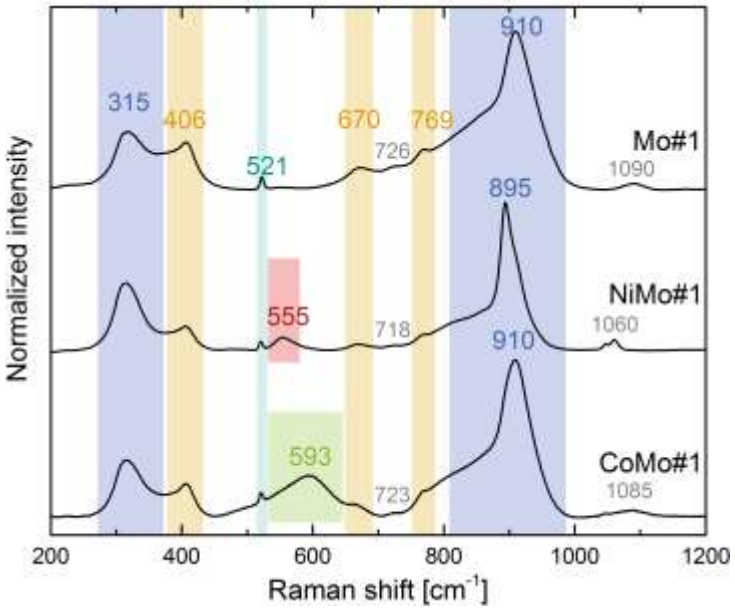

Figure 7 Baseline corrected Raman spectra of Mo#1, NiMo#1, and CoMo#1 in the oxide phase (calcined, not dehydrated, see Table 1). The Raman bands were assigned to monomolybdate tetrahedral (blue: 315,895, 910 cm^{-1}), the $MgAl_2O_4$ support (orange: 406, 670, 769 cm^{-1}), supported and dispersed NiO (red: 555 cm^{-1}), supported CoO (green: 593 cm^{-1}), and Si impurities (turquoise: 521 cm^{-1}).

The presence of highly dispersed MoO_x was also verified by XAS. Figure 8 shows XANES spectra of the dehydrated and sulfided Mo#1 along with references, which exhibit different features depending on the oxidation state and coordination geometry of the central Mo atom. Similar XANES spectra of dehydrated and sulfided NiMo#1 and CoMo#1 at the respective Mo, Ni, and Co K-edges are given in the supplementary information, Figure S.4. The XANES spectrum of the dehydrated sample exhibits a pre-edge peak at ≈ 20,005 eV indicating the presence of Mo^{6+} (see Figure 8). This pre-edge peak, which was seen for all dehydrated samples, is quite intense, which further indicates tetrahedral geometry around the central Mo atom [87,88].

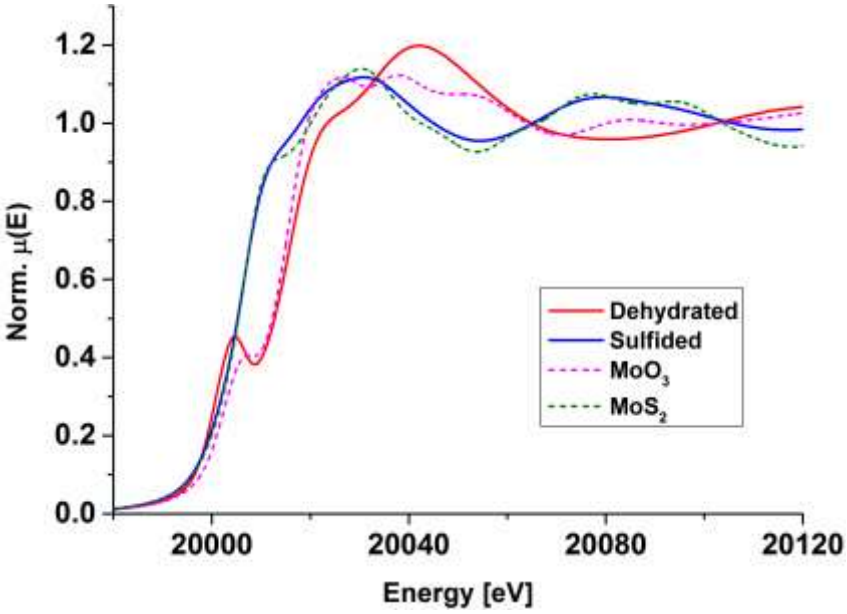

Figure 8 Mo K-edge XANES spectra of the dehydrated and sulfided Mo#1 together with MoO_3 and MoS_2 references.

The EXAFS fitting results obtained at the Mo K-edge for all dehydrated samples are shown in Table 3. The corresponding Fourier transformed (FT) spectra with fitted theoretical models are given in the supplementary information, Figure S.5-FigureS.6 (Mo K-edge) and Figure S.7 (Ni K-edge and Co K-edge). For the dehydrated samples, the CN of Mo-O was found in the range of 4.2-4.6 with an average bond length of 1.75 Å, which is in accordance with the XANES results. Higher metal-metal shells were not observed in the FT spectra of these samples indicating high dispersion as also found by Raman spectroscopy.

Table 3 Mo K-edge EXAFS fitting results for the dehydrated oxide phase precursors. Δ states the uncertainty in the reported values.

	Mo-O		
Catalyst	**R [Å]**	**CN (ΔCN) [-]**	**σ^2 ($\Delta\sigma^2$) [$Å^{-2}$]·10^3**
Mo#1	1.76	4.2(0.4)	4.9(0.7)
NiMo#1	1.73	4.6(0.7)	5.8(1.6)
CoMo#1	1.75	4.3(0.4)	5.1(0.7)

3.5.2. Oxide to Sulfide Conversion during Sulfidation

The transition of oxide to sulfide was followed in-situ with XANES and EXAFS (see Figure 9 and Figure 10). Similarly to what has been obtained in literature [89–92], the oxide precursor underwent transformation into intermediate oxy-sulfide species prior to conversion into the final sulfide form.

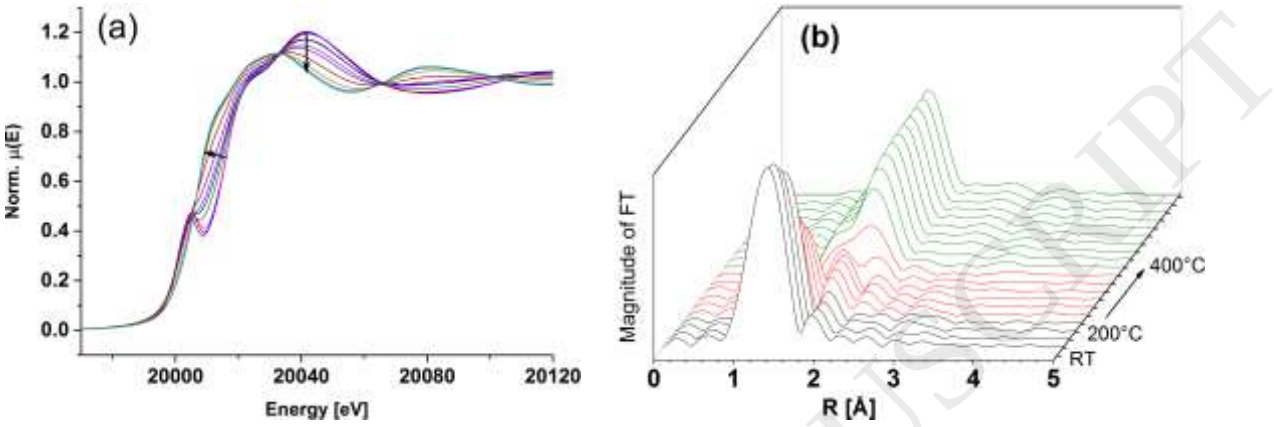

Figure 9 Mo K-edge XAS results as (a) XANES spectra and (b) corresponding magnitude of the FT (fitted k^3-weighted EXAFS spectra) for in-situ sulfidation of Mo#1. (a) Overlaid view; arrows indicate change over time. (b) Averaged magnitude of FT spectra are shown as a function of time indicating presence of oxide (black), intermediate oxy-sulfide (red), and sulfide (green) phases.

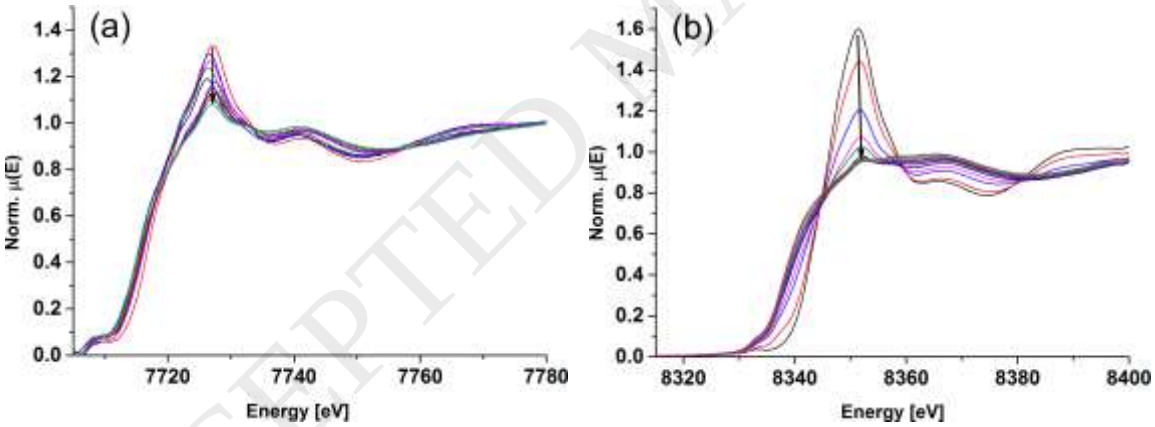

Figure 10 XANES spectra for in-situ sulfidation of (a) CoMo#1 at the Co K-edge and (b) NiMo#1 at the Ni K-edge; arrows indicate change over time.

A linear combination fitting (LCF) analysis of the XANES spectra obtained during sulfidation of the three catalysts (Mo#1, NiMo#1, CoMo#1) showed that Ni promotion increased the rate of sulfidation (see Figure 11). Based on the Mo K-edge spectra, 10 % oxide phase remained at ≈ 320 °C in Mo, at ≈ 335 °C in CoMo, and at ≈ 295 °C in NiMo (Figure 11a-c). Looking at the promotor

K-edges, 10 % Co oxide phase remained at ≈ 335 °C, whereas 10 % Ni oxide phase remained at ≈ 260 °C (Figure 11d-e). Thus, Ni was sulfided faster than Mo and this aided the sulfidation of Mo, whereas Co had no significant influence on the sulfidation rate of Mo.

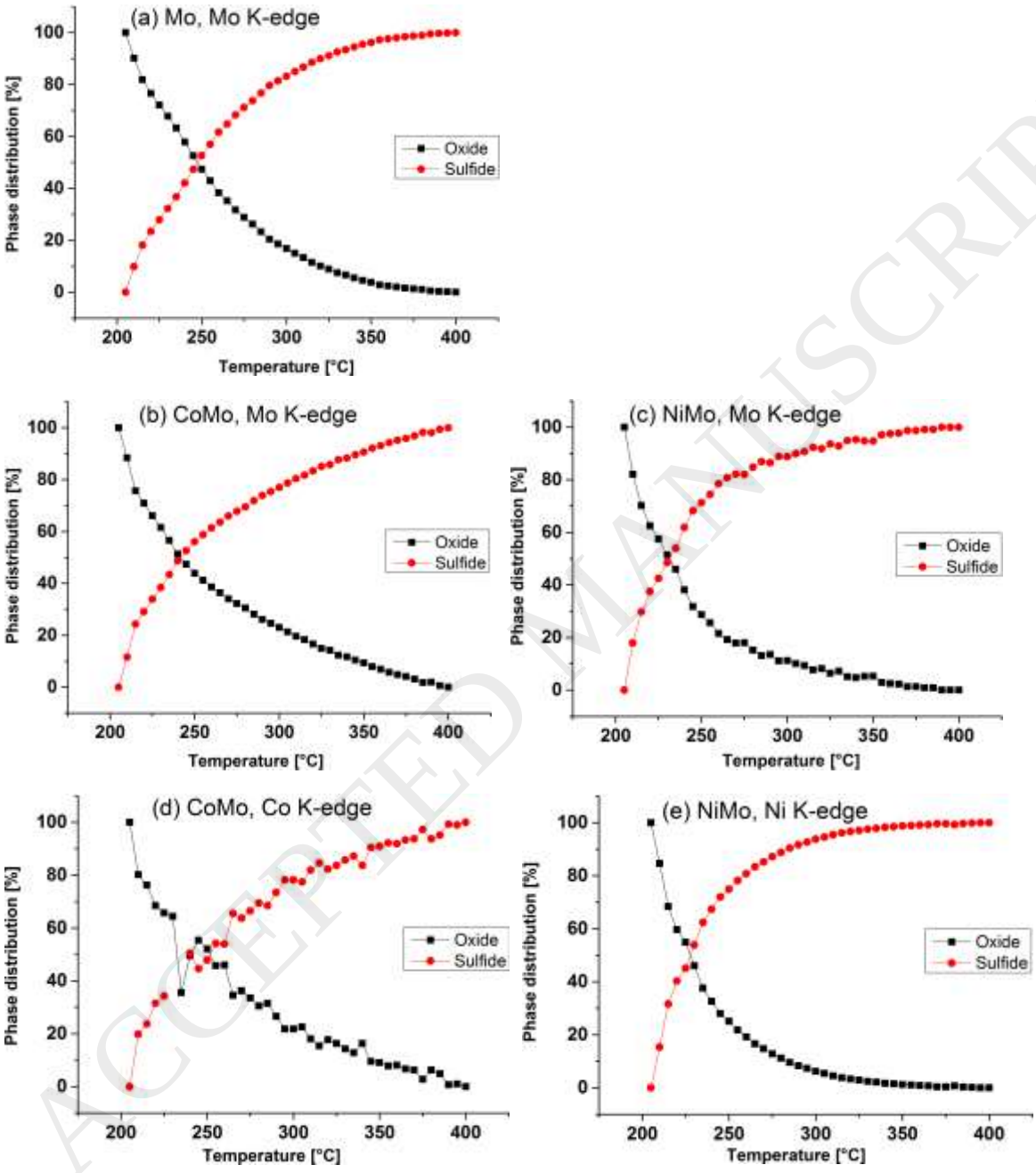

Figure 11 LCF analysis of fitted EXAFS spectra from in-situ sulfidation at the Mo K-edge for (a) Mo#1, (b) CoMo#1, (c) NiMo#1, at the Co K-edge for (d) CoMo#1, and at the Ni K-edge for (e) NiMo#1.

3.5.3. Sulfide Phase

The presence of small and highly dispersed MoS_2 particles was revealed by EXAFS. The structural parameters determined from fitting the Mo K-edge spectra of the sulfided catalysts and at the promotor K-edges spectra for the dehydrated and sulfided samples are shown in Table 4.

Table 4 EXAFS fitting results. Mo K-edge results for all three sulfided catalysts and Ni and Co K-edge results for dehydrated and sulfided NiMo#1 and CoMo#1. Δ states the uncertainty in the reported values.

K-edge/ catalyst	**R [Å]**	**CN (ΔCN) [-]**	**σ^2 ($\Delta\sigma^2$) [Å^{-2}]·10^3**	**R [Å]**	**CN (ΔCN) [-]**	**σ^2 ($\Delta\sigma^2$) [Å^{-2}]·10^3**	**R [Å]**	**CN (ΔCN) [-]**	**σ^2 ($\Delta\sigma^2$) [Å^{-2}]·10^3**
Mo K-edge /	**Mo-O**			**Mo-S**			**Mo-Mo**		
Mo#1	1.65	0.19(0.07)	4.9(0.7)[a]	2.40	4.1(0.2)	8.4(0.5)	3.16	0.40(0.07)	3.2(0.2)[b]
NiMo#1	1.62	0.32(0.11)	4.9(0.7)[a]	2.40	4.8(0.3)	8.9(0.6)	3.17	0.43(0.10)	3.2(0.2)[b]
CoMo#1	1.64	0.32(0.11)	4.9(0.7)[a]	2.41	4.4(0.4)	9.8(0.9)	3.17	0.26(0.09)	3.2(0.2)[b]
Ni K-edge /	**Ni-O**			**Ni-Ni**			**Ni-Mo**		
Dehydrated	2.04	5.4(0.7)	7.7(1.4)	3.20	3.0(-)[c]	6.7(2.8)	3.20	3.0(-)[c]	6.7(2.8)
	Ni-S			**Ni-Ni**			**Ni-Mo**		
Sulfided	2.22	3.60(0.6)	8.6(1.8)	2.83	1.0(-)[c]	7.8(4.4)	3.30	1.0(-)[c]	5.7(1.4)
Co K-edge /	**Co-O**								
Dehydrated	1.92	4.5(1.1)	3.1(2.0)						
	Co-S			**Co-Co (1st)**			**Co-Mo**		
Sulfided	2.16	2.54(0.55)	6.1(1.8)	2.53	3.0(-)[c]	13.3(1.7)	3.81	2.0(-)[c]	5.7(3.3)
				Co-Co (2nd)					
				3.85	3.0(-)[c]	9.0(0.6)			

a) $\Delta\sigma^2$ for Mo-O was fixed to the value as determined from dehydrated Mo#1 sample.
b) $\Delta\sigma^2$ for Mo-Mo was fixed to the value as determined from a MoS_2 reference.
c) The parameter was fixed during the fitting.

The Mo K-edge results show that all three sulfided catalysts had a Mo-O contribution at 1.62-1.65 Å with a very low CN of 0.19-0.32 (see Table 4). This may be explained by an interaction with the support resulting in the formation of highly dispersed, small particles as indicated by Raman. The very low CN observed for the Mo-O coordination, indicates that there is no actual bonding between Mo and O but only a slight interaction. In a recent study, Rochet et al. [89] also reported a very short Mo-O contribution at 1.68 Å with a CN of 1, which was proposed to be due to the presence of molybdenum oxysulfide species. In our case, the Mo-O CN is too low to predict the formation of such phases. Furthermore, Rochet et al. [89] observed a weak pre-edge feature in the XANES spectrum corresponding to the presence of molybdenum oxide species. In the sulfided samples of

this work, however, no such peak was observed. Thus, most probably the short Mo-O bond with very low CN was due to interaction with the support.

The Mo-S coordination at 2.40-2.41 Å with a CN of 4.1-4.8 corresponds to the MoS_2 phase and is in agreement with published values [56,90,93]. The Mo-Mo coordination at 3.16-3.17 Å also corresponds to literature results [56,90], but the CN = 0.26-0.43 is too low to obtain a precise estimate of the particle size (e.g. due to high temperature leading to a high Debye-Waller factor and small particle size due to mobility at > 300 °C), which is expected to be < 2 nm [93]. A TEM analysis was performed (see supplementary information, Figure S.13 and Figure S.14) giving an average slab length of 4.3±2.8 nm with a mean stacking of 1.2. But with an average Mo-Mo CN < 1 from EXAFS, the majority of the particles were too small (< 2 nm) to detect with TEM at the applied resolution. These results are in line with the findings of Seo and Lee [94], who showed that the formation of MoS_2 particles can take place through the initial formation of nanoparticles of ≤ 1 nm at mild sulfidation conditions. No Mo-Mo backscattering at 3.16 Å was detected for these particles indicating a very low coordination number, but at the same time, a Mo-S signal at 2.4 Å with a CN of 3.6 was reported, and the elemental S/Mo ratio was 1.3 [94]. As the sulfidation temperature was increased, they showed (TEM and EXAFS) that the nanoparticles merged to form the well-known MoS_2 slab structures giving stronger Mo-Mo backscattering. In this work, a low Mo loading (sub monolayer, see Table 1) and rather mild sulfidation conditions were applied; i.e. moderate temperature and low pressure. Together with a strong support interaction as indicated by the Mo-O contribution at 1.62-1.65 Å, this is proposed to have caused the formation of very small and highly dispersed MoS_2 particles.

Using the EXAFS results (Table 4), a MoS_2 cluster was constructed from a bulk MoS_2 model by only including the first shell of S and a single Mo atom from the second Mo shell. The central Mo atom thus had a Mo-S CN of 6, similar to bulk MoS_2, and a Mo-Mo CN of 1. The outer Mo atom

had a Mo-S CN of 2 and a Mo-Mo CN of 1, which gives an average Mo-S CN of 4, corresponding to the EXAFS results (see Table 4), and Mo-Mo CN of 1. The structure of this cluster is shown in the supplementary information, Figure S.8. FEFF9 simulations were performed with each of the two Mo atoms as the absorber, and the obtained spectra were averaged to get the XANES spectrum shown in Figure 12. The Debye-Waller factor obtained from the EXAFS fitting was used to introduce the disorder in the model. The spectra were averaged with a 1:1 ratio between the two Mo atoms, which gave a good agreement between modelled and experimental XANES spectra and supported the EXAFS results (see Figure 12). There are, however, some regions where the shape of the modelled spectrum deviates from the experimental spectrum, possibly due to presence of further contributions from Mo-S and Mo-Mo in the sample not considered in the model.

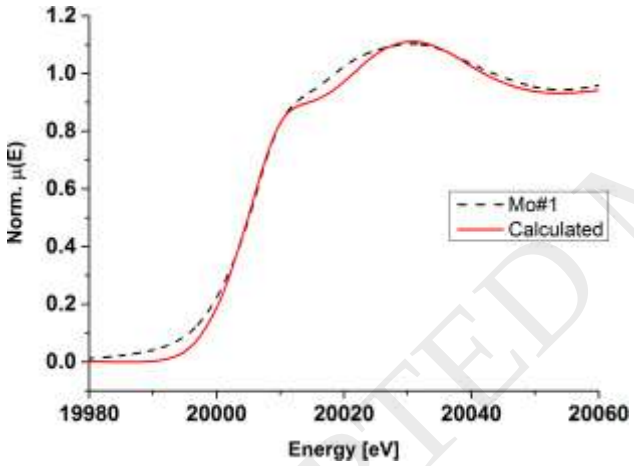

Figure 12 XANES spectrum for sulfided Mo#1 together with the average calculated XANES spectrum (FEFF9) for a MoS_2 cluster consisting of two Mo atoms and with an average Mo-S CN of 4 and an average Mo-Mo CN of 1.

The EXAFS results obtained at the Co K-edge indicate that a bulk Co_9S_8 phase was present in the sulfided CoMo catalyst (see Table 4). The Co-S CN of 2.54 with bond length 2.16 Å is similar to one of the shorter Co-S coordinations present in Co_9S_8 [95], and the low CN of 2.54 indicates the presence of smaller particles on the surface. The presence of a Co-Co shell was observed at a higher distance of 3.85 Å supporting presence of a Co_9S_8 phase after sulfidation [95]. Also, a Co-Mo shell

was found at about the same distance of 3.81 Å indicating that some Co atoms were replaced by Mo, which points towards the presence of a CoMoS phase. Thus, the sulfided phase in the CoMo catalyst seemed to contain a mixture of Co_9S_8 and CoMoS.

Especially CoMo catalysts have been reported to be sensitive towards bulk Co_9S_8 formation during sulfidation with the propensity to form this undesired phase being dependent on the catalyst preparation method. Co_9S_8 is most likely to form in samples prepared from a stepwise incipient wetness impregnation where the Co precursor has been added prior to the Mo precursor [13]. Co_9S_8 formation can be minimized by application of a chelating agent, such as citric acid, to the impregnation solution, which has been reported to stabilize Co and Mo precursors at the catalyst surface and facilitate a high degree of promotion of Co in the resulting MoS_2 structure [56,90,96]. The catalytic activity repeatability test (see section 3.3.1 and Figure 6) might thus be improved by altering the catalyst preparation procedure.

For NiMo, the EXAFS results obtained at the Ni K-edge indicated the presence of a NiMoS phase. The Ni-S CN of 3.60 with bond length 2.22 Å is similar to the results obtained by Rochet et al. [97] for a sulfided $NiMo/Al_2O_3$ catalyst, which was prepared with approximately the same metal loading per nm^2 available support surface area as for this work. The Ni K-edge XANES spectrum for the sulfided catalyst (see supplementary information, Figure S.4), showed similar features as the NiMoS XANES spectrum reported in literature [98]. Furthermore, a small bump at ≈ 8352 eV corresponded to the white line characteristics of $NiAl_2O_4$ indicating some interaction of Ni with the $MgAl_2O_4$ support.

3.5.4. Stability against Varying H_2O/H_2S

The stability of promoted and unpromoted MoS_2 against H_2O/H_2S variations was investigated in-situ by XAS. After sulfidation, the catalysts were exposed to different molar ratios of H_2O/H_2S (30, 100, 190, and 300) corresponding to 100-500 ppm H_2S and 1.6-3.0 % H_2O. In the performed

activity tests (Figure 4 and Figure 5), full conversion corresponded to a H_2O/H_2S ratio of ≈ 125 and ≈ 30 at 550 and 2200 ppm H_2S, respectively.

Figure 13 shows the in-situ XANES spectra at the Mo K-edge for Mo#1, CoMo#1, and NiMo#1, at the Co K-edge for CoMo#1, and at the Ni K-edge for NiMo#1, respectively, during H_2O/H_2S variations. Any changes induced by adding water to the gas and increasing the H_2O/H_2S ratio were negligible, which indicates that all catalysts were stable against water induced phase change such as oxidation for H_2O/H_2S ratios ≤300. Also, the variation in the EXAFS parameters for the catalysts exposed to H_2O were too small to predict any phase transformation and are hence not presented here.

The presence of promotors in the CoMo and NiMo catalysts could stabilize the catalyst against oxidation as indicated by the DFT results (see Figure 2), which suggested a lower stability of unpromoted MoS_2, but at the same time only provided general trends. Furthermore, the stability could be due to a stabilizing effect from the strong interaction between the small and highly dispersed particles with the support. A possibility for further investigating the influence of H_2O/H_2S variations could be to perform modulation excitation spectroscopy (MES) during in-situ experiments, which can potentially enhance the sensitivity of small and fast changes [99]. This is outside the scope of this paper, and it is the topic of further research.

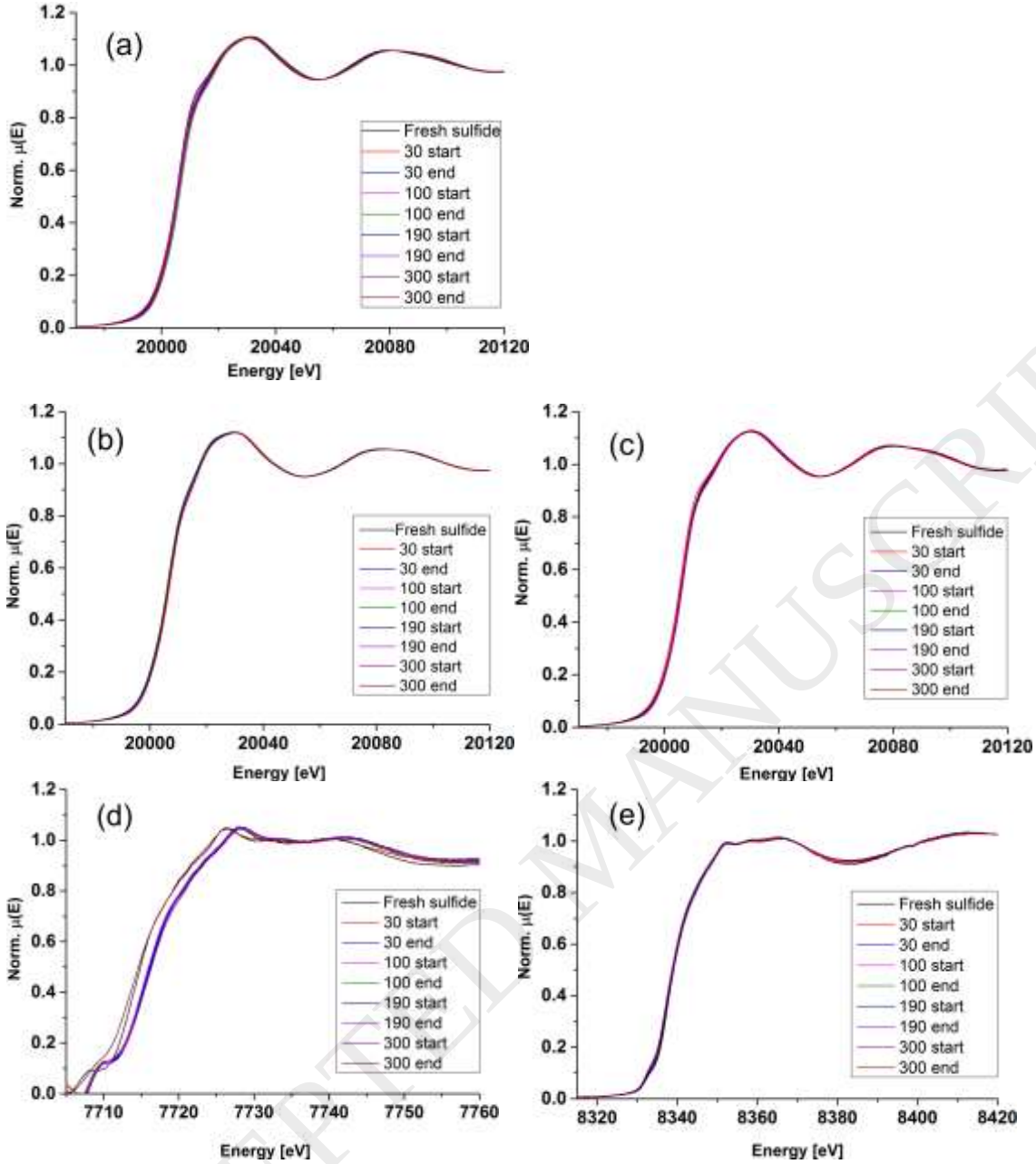

Figure 13 Average XANES spectra from in-situ H_2O/H_2S variations at the Mo K-edge for (a) Mo#1, (b) CoMo#1, (c) NiMo#1, (d) at the Co K-edge for CoMo#1, and (e) at the Ni K-edge for NiMo#1. Numbers indicate molar H_2O/H_2S ratios. Start and end denote whether the averaged XANES spectra are from the first or last 5 minutes of the exposure time at the given ratio.

3.6. Target Sulfide Phase for HDO at Elevated Temperature

A strong support interaction (commonly through Mo-O-Al linkages) has often been associated with formation of the less active type I sulfide phases [56,90,96]. Type I sulfides are smaller particles with higher dispersion than type II sulfides that more resemble bulk MoS_2 [100]. A moderately active catalyst stabilized through the support interaction of highly dispersed MoS_2 particles was the aim in this work, where a catalyst for in-situ HDO of pyrolysis vapors at high temperatures (≈ 500 °C) is targeted. If a too active catalyst (such as type II sulfides) is prepared, extensive cracking can minimize (potentially remove) the oil yield when a real biomass feed is used. Additionally, the strong active phase-support interaction helps in stabilizing the active phase upon water exposure, this could further favor the use of type I sulfides in high temperature HDO of pyrolysis vapor.

A bulk-like MoS_2 structure with a Mo-S CN of ≈ 6 can be obtained by lowering the interaction with the support; either by the use of a chelating agent during impregnation on Mo-O-Al anchoring supports such as Al_2O_3 [56,90,96], or by the use of an inert support such as carbon [96]. Sulfidation conditions (temperature, pressure, and sulfur source) can additionally be used to alter the composition of formed sulfides [56,90,100,101]. As mentioned, the loading of Mo also influences the type I/II distribution as a higher loading minimized the support interaction and favors the formation of fully sulfided MoS_2 with Mo-S CN = 6 [13,55].

It has been reported that NiMo catalysts are more active for HDO of aliphatic species, while CoMo catalysts are more active for HDO of aromatic species [29,44,45,102]. In this work, similar activities were seen with the prepared NiMo and CoMo catalysts tested for ethylene glycol conversion. Biomass fast pyrolysis vapor will contain both aliphatic and aromatic oxygenates. It could therefore be interesting to test the activity and stability of the prepared catalysts for HDO of aromatic species. Mixtures of aromatic and aliphatic species should be tested as well to study possible competitive inhibition. However, the aliphatic oxygenates (sugar derived polyols, ketones,

acids, and aldehydes) are responsible for the most detrimental properties of bio-oil. These species should be upgraded by HDO immediately when formed during catalytic hydropyrolysis. Further upgrading of more refractory aromatic species could potentially be performed downstream in a fixed bed reactor operating with another catalyst at other operating conditions.

4. Conclusions

DFT, catalytic activity tests, and in-situ XAS was conducted to provide detailed information on the activity and stability of MoS_2, Ni-MoS_2, and Co-MoS_2 catalysts used for HDO upon variation of the partial pressures of H_2O and H_2S. H_2S was added to the reaction gas to stabilize the sulfide catalyst, while H_2O is a HDO reaction product. DFT calculations showed that the active edge of MoS_2 could be stabilized against S-O exchanges by increasing the partial pressure of H_2S or by promotion with either Ni or Co. HDO activity tests were performed using Mo, NiMo, and CoMo catalysts prepared by incipient wetness impregnation using a $MgAl_2O_4$ support. Ethylene glycol was chosen as a model compound representing the more reactive cellulose derived species formed during pyrolysis of biomass. The prepared MoS_2 based catalysts were all active and fairly selective for ethylene glycol HDO at 400 °C, 27 bar H_2, and 550-2200 ppm H_2S, and produced ethane, ethylene, and C_1 cracking products at C_2/C_1 ratios of 1.5-4.8 and conversions of ≈ 50-100 %. Both DFT and catalytic activity tests indicated that increasing the H_2S concentration in the gas increased the concentration of SH groups on the catalyst, which correspondingly activated and stabilized the catalytic HDO performance. In-situ XAS showed that the catalysts were tolerant towards water, and that the active phases were present as small and highly dispersed particles.

Acknowledgements

This work is part of the H_2CAP (hydrogen assisted catalytic pyrolysis for green fuels) project conducted at The Department of Chemical and Biochemical Engineering at DTU, Denmark. The work was supported by The Danish Council for Strategic Research (now: Innovation Fund Denmark) project 1377-00025A, The Programme Commission on Sustainable Energy and Environment. Tim Prüßmann and Alexey Boubnov (KIT) aided the XAS studies. KIT and DFG financed the Raman spectrometer (INST 121384/73-1). Haldor Topsøe A/S performed the elemental analysis and some of the BET analysis. Analysis of TEM micrographs was performed by Simon B. Lindahl and Mads L. Andersen (DTU Chemical and Biochemical Engineering). The technicians and workshop at DTU Chemical and Biochemical Engineering have assisted the construction and maintenance of the experimental setup used for catalytic activity tests.

The supplementary information contains N_2 physisorption results, GC-MS analysis details, in-situ XAS experimental procedure, EXAFS fitting procedure and results, detailed TOS profiles from the catalytic activity tests, Raman curve fitting results, as well as TEM analysis.

Conflicts of interest: none.

References

[1] Core Writing Team, R.K. Pachauri, L.A. Meyers, Climate Change 2014: Synthesis Report, IPCC, Geneva, 2014.

[2] M. Balat, Energy Convers. Manag. 52 (2011) 858–875.

[3] A. Roedl, Int. J. Life Cycle Assess. 15 (2010) 567–578.

[4] P. McKendry, Bioresour. Technol. 83 (2002) 37–46.

[5] A.V. Bridgwater, Biomass and Bioenergy 38 (2012) 68–94.

[6] P.C. Badger, P. Fransham, Biomass and Bioenergy 30 (2006) 321–325.

[7] K. Raffelt, E. Henrich, A. Koegel, R. Stahl, J. Steinhardt, F. Weirich, Appl. Biochem. Biotechnol. 129–132 (2006) 153–164.

[8] A. Oasmaa, S. Czernik, Energy & Fuels 13 (1999) 914–921.

[9] S. Albertazzi, F. Basile, G. Fornasari, F. Trifirò, A. Vaccari, Chapter 7: Thermal Biomass Conversion, Catalysis for Renewables: From Feedstock to Energy Production, Wiley-VCH Verlag GmbH & Co. KGaA, Weinheim, 2007.

[10] A.M. Azeez, D. Meier, J. Odermatt, T. Willner, Energy & Fuels 24 (2010) 2078–2085.

[11] C. Boscagli, K. Raffelt, T.A. Zevaco, W. Olbrich, T.N. Otto, J. Sauer, J.-D. Grunwaldt, Biomass and Bioenergy 83 (2015) 525–538.

[12] L. Negahdar, A. Gonzalez-Quiroga, D. Otyuskaya, H.E. Toraman, L. Liu, J.T.B.H. Jastrzebski, K.M. Van Geem, G.B. Marin, et al., ACS Sustain. Chem. Eng. 4 (2016) 4974–4985.

[13] H. Topsøe, B.S. Clausen, F.E. Massoth, Hydrotreating Catalysis, Volume 11, Springer-Verlag, Berlin Heidelberg, Germany, 1996.

[14] T. Cordero-Lanzac, R. Palos, J.M. Arandes, P. Castaño, J. Rodríguez-Mirasol, T. Cordero, J. Bilbao, Appl. Catal. B Environ. 203 (2017) 389–399.

[15] W. Baldauf, U. Balfanz, M. Rupp, Biomass and Bioenergy 7 (1994) 237–244.

[16] D.C. Elliott, T.R. Hart, G.G. Neuenschwander, L.J. Rotness, A.H. Zacher, Environ. Prog. Sustain. Energy 28 (2009) 441–449.

[17] Y. Wang, H. Lin, Y. Zheng, Catal. Sci. Technol. 4 (2014) 109–119.

[18] J. Wildschut, F.H. Mahfud, R.H. Venderbosch, H.J. Heeres, Ind. Eng. Chem. Res. 48 (2009) 10324–10334.

[19] Y.-H.E. Sheu, R.G. Anthony, E.J. Soltes, Fuel Process. Technol. 19 (1988) 31–50.

[20] D.C. Elliott, Energy & Fuels 21 (2007) 1792–1815.

[21] S. Czernik, D.K. Johnson, S. Black, Biomass and Bioenergy 7 (1994) 187–192.

[22] A. Oasmaa, E. Kuoppala, Energy & Fuels 17 (2003) 1075–1084.

[23] M. Linck, L. Felix, T. Marker, M. Roberts, WIREs Energy Environ. 3 (2014) 575–581.

[24] F.L.P. Resende, Catal. Today 269 (2016) 148–155.

[25] V.N. Bui, D. Laurenti, P. Afanasiev, C. Geantet, Appl. Catal. B Environ. 101 (2011) 239–245.

[26] M. Badawi, J.-F. Paul, S. Cristol, E. Payen, Catal. Commun. 12 (2011) 901–905.

[27] A. Centeno, E. Laurent, B. Delmon, J. Catal. 154 (1995) 288–298.

[28] E. Laurent, B. Delmon, Appl. Catal. A Gen. 109 (1994) 97–115.

[29] O.İ. Şenol, T.-R. Viljava, A.O.I. Krause, Appl. Catal. A Gen. 326 (2007) 236–244.

[30] E.-M. Ryymin, M.L. Honkela, T.-R. Viljava, A.O.I. Krause, Appl. Catal. A Gen. 389 (2010) 114–121.

[31] V.N. Bui, D. Laurenti, P. Delichère, C. Geantet, Appl. Catal. B Environ. 101 (2011) 246–255.

[32] A. Gutierrez, E.-M. Turpeinen, T.-R. Viljava, O. Krause, Catal. Today 285 (2017) 125–134.

[33] C. Bouvier, Y. Romero, F. Richard, S. Brunet, Green Chem. 13 (2011) 2441–2451.

[34] P.M. Mortensen, J.-D. Grunwaldt, P.A. Jensen, K.G. Knudsen, A.D. Jensen, Appl. Catal. A Gen. 407 (2011) 1–19.

[35] E. Furimsky, Appl. Catal. A Gen. 199 (2000) 147–190.

[36] R.H. Venderbosch, A.R. Ardiyanti, J. Wildschut, A. Oasmaa, H.J. Heeres, J. Chem. Technol. Biotechnol. 85 (2010) 674–686.

[37] P.M. de Souza, R.C. Rabelo-Neto, L.E.P. Borges, G. Jacobs, B.H. Davis, T. Sooknoi, D.E. Resasco, F.B. Noronha, ACS Catal. 5 (2015) 1318–1329.

[38] P.M. Mortensen, J.-D. Grunwaldt, P.A. Jensen, A.D. Jensen, ACS Catal. 3 (2013) 1774–1785.

[39] T.N. Trinh, P.A. Jensen, K. Dam-Johansen, N.O. Knudsen, H.R. Sørensen, S. Hvilsted, Energy & Fuels 27 (2013) 1399–1409.

[40] E. Laurent, B. Delmon, J. Catal. 146 (1994) 281–291.

[41] M. Badawi, J.-F. Paul, S. Cristol, E. Payen, Y. Romero, F. Richard, S. Brunet, D. Lambert, et al., J. Catal. 282 (2011) 155–164.

[42] P.M. Mortensen, PhD Thesis: Catalytic Conversion of Bio-Oil to Fuel for Transportation, Technical University of Denmark, Dept. of Chemical and Biochemical Engineering, 2013.

[43] M. Badawi, S. Cristol, J.-F. Paul, E. Payen, C.R. Chim. 12 (2009) 754–761.

[44] O.İ. Şenol, T.-R. Viljava, A.O.I. Krause, Catal. Today 106 (2005) 186–189.

[45] O.İ. Şenol, E.-M. Ryymin, T.-R. Viljava, A.O.I. Krause, J. Mol. Catal. A Chem. 277 (2007) 107–112.

[46] P.G. Moses, B. Hinnemann, H. Topsøe, J.K. Nørskov, J. Catal. 268 (2009) 201–208.

[47] J.V. Lauritsen, F. Besenbacher, J. Catal. 328 (2015) 49–58.

[48] A. Travert, H. Nakamura, R.A. van Santen, S. Cristol, J.-F. Paul, E. Payen, J. Am. Chem. Soc. 124 (2002) 7084–7095.

[49] P. Giannozzi, S. Baroni, N. Bonini, M. Calandra, R. Car, C. Cavazzoni, D. Ceresoli, G.L. Chiarotti, et al., J. Phys. Condens. Matter 21 (2009) 395502.

[50] J. Wellendorff, K.T. Lundgaard, A. Møgelhøj, V. Petzold, D.D. Landis, J.K. Nørskov, T. Bligaard, K.W. Jacobsen, Phys. Rev. B 85 (2012) 235149.

[51] J.B. Varley, Y. Wang, K. Chan, F. Studt, Phys. Chem. Chem. Phys. 17 (2015) 29541–29547.

[52] H.J. Monkhorst, J.D. Pack, Phys. Rev. B 13 (1976) 5188–5192.

[53] M. V. Bollinger, K.W. Jacobsen, J.K. Nørskov, Phys. Rev. B 67 (2003) 85410.

[54] S. Houssenbay, E. Payen, S. Kasztelan, J. Grimblot, Catal. Today 10 (1991) 541–560.

[55] J.A.R. van Veen, E. Gerkema, A.M. van der Kraan, P.A.J.M. Hendriks, H. Beens, J. Catal. 133 (1992) 112–123.

[56] L. Medici, R. Prins, J. Catal. 163 (1996) 38–49.

[57] H. Hu, I.E. Wachs, S.R. Bare, J. Phys. Chem 99 (1995) 10897–10910.

[58] J. Strunk, M.A. Bañares, I.E. Wachs, Top Catal (2017) Published online: DOI 10.1007/s11244-017-0841-x.

[59] K. Schofield, Prog. Energy Combust. Sci. 34 (2008) 330–350.

[60] O. Müller, M. Nachtegaal, J. Just, D. Lützenkirchen-Hecht, R. Frahm, J. Synchrotron Rad 23 (2016) 260–266.

[61] J.-D. Grunwaldt, M. Caravati, S. Hannemann, A. Baiker, Phys. Chem. Chem Phys. 6 (2004) 3037–3047.

[62] B.S. Clausen, G. Steffensen, B. Fabius, J. Villadsen, R. Feidenhans'l, H. Topsøe, J. Catal. 132 (1991) 524–535.

[63] B. Ravel, M. Newville, J. Synchrotron Rad. 12 (2005) 537–541.

[64] J.J. Rehr, J.J. Kas, F.D. Vila, M.P. Prange, K. Jorissen, Phys. Chem. Chem Phys. 12 (2010) 5503–5513.

[65] A. Gaur, B.D. Shrivastava, J. Phys. Conf. Ser. 534 (2014) 1–5.

[66] J.V. Lauritsen, M.V. Bollinger, E. Lægsgaard, K.W. Jacobsen, J.K. Nørskov, B.S. Clausen, H. Topsøe, F. Besenbacher, J. Catal. 221 (2004) 510–522.

[67] J.V. Lauritsen, S. Helveg, E. Lægsgaard, I. Stensgaard, B.S. Clausen, H. Topsøe, F. Besenbacher, J. Catal. 197 (2001) 1–5.

[68] J.V. Lauritsen, J. Kibsgaard, G.H. Olesen, P.G. Moses, B. Hinnemann, S. Helveg, J.K. Nørskov, B.S. Clausen, et al., J. Catal. 249 (2007) 220–233.

[69] M. Brorson, A. Carlsson, H. Topsøe, Catal. Today 123 (2007) 31–36.

[70] F. Besenbacher, M. Brorson, B.S. Clausen, S. Helveg, B. Hinnemann, J. Kibsgaard, J.V. Lauritsen, P.G. Moses, et al., Catal. Today 130 (2008) 86–96.

[71] A. Popov, E. Kondratieva, J.M. Goupil, L. Mariey, P. Bazin, J.-P. Gilson, A. Travert, F. Maugé, J. Phys. Chem. C 114 (2010) 15661–15670.

[72] R.C. Runnebaum, T. Nimmanwudipong, D.E. Block, B.C. Gates, Catal. Sci. Technol. 2 (2012) 113–118.

[73] J. Towfighi, M. Sadrameli, A. Niaei, J. Chem. Eng. Japan 35 (2002) 923–937.

[74] M.R. de Brimont, C. Dupont, A. Daudin, C. Geantet, P. Raybaud, J. Catal. 286 (2012) 153–164.

[75] J.V. Lauritsen, M. Nyberg, J.K. Nørskov, B.S. Clausen, H. Topsøe, E. Lægsgaard, F. Besenbacher, J. Catal. 224 (2004) 94–106.

[76] J.V. Lauritsen, M. Nyberg, R.T. Vang, M.V. Bollinger, B.S. Clausen, H. Topsøe, K.W. Jacobsen, E. Lægsgaard, et al., Nanotechnology 14 (2003) 385–389.

[77] N.-Y. Topsøe, H. Topsoe, J. Catal. 139 (1993) 641–651.

[78] J. Medema, C. van Stam, V.H.J. de Beer, A.J.A. Konings, K.D. C, J. Catal. 53 (1978) 386–400.

[79] V. D'Ippolito, G.B. Andreozzi, D. Bersani, P.P. Lottici, J. Raman Spectrosc. 46 (2015) 1255–1264.

[80] M.A. Vuurman, D.J. Stufkens, A. Oskam, G. Deo, I.E. Wachs, J. Chem. Soc. Faraday Trans. 92 (1996) 3259–3265.

[81] E. Payen, M.C. Dhamelincourt, P. Dhamelincourt, J. Grimblot, J.P. Bonnelle, Appl. Spectrosc. 36 (1982) 30–37.

[82] H.M. Abdel-Dayem, Ind. Eng. Chem. Res. 46 (2007) 2466–2472.

[83] H. Ohtsuka, T. Tabata, O. Okada, L.M.F. Sabatino, G. Bellussi, Catal. Letters 44 (1997) 265–270.

[84] B. Jongsomjit, J. Panpranot, J.G. Goodwin, J. Catal. 204 (2001) 98–109.

[85] S.I. Cordoba-Torresi, A.H. Goff, S. Joiret, J. Electrochem. Soc. 138 (1991) 1554–1559.

[86] G. Mestl, T.K.K. Srinivasan, Catal. Rev. 40 (1998) 451–570.

[87] A.M. Beale, G. Sankar, Chem. Mater. 15 (2003) 146–153.

[88] A. Tougerti, E. Berrier, A.-S. Mamede, C. La Fontaine, V. Briois, Y. Joly, E. Payen, J.-F. Paul, et al., Angew. Chemie Int. Ed. 52 (2013) 6440–6444.

[89] A. Rochet, B. Baubet, V. Moizan, C. Pichon, V. Briois, C.R. Chim. 19 (2016) 1337–1351.

[90] L. van Haandel, G.M. Bremmer, E.J.M. Hensen, T. Weber, J. Catal. 342 (2016) 27–39.

[91] L. van Haandel, E.J.M. Hensen, T. Weber, Catal. Today 292 (2017) 51–57.

[92] R. Cattaneo, T. Weber, T. Shido, R. Prins, J. Catal. 191 (2000) 225–236.

[93] T. Shido, R. Prins, J. Phys. Chem. B 102 (1998) 8426–8435.

[94] H.-R. Seo, Y.-K. Lee, J. Korean Phys. Soc. 59 (2011) 730–734.

[95] S.M.A.M. Bouwens, J.A.R. van Veen, D.C. Koningsberger, V.H.J. de Beer, R. Prins, J. Phys. Chem. 95 (1991) 123–134.

[96] E.J.M. Hensen, V.H.J. de Beer, J.A.R. van Veen, R.A. van Santen, Catal. Letters 84 (2002) 59–67.

[97] A. Rochet, B. Baubet, V. Moizan, E. Devers, A. Hugon, C. Pichon, E. Payen, V. Briois, J. Phys. Chem. C 119 (2015) 23928–23942.

[98] Y. Hamabe, S. Jung, H. Suzuki, N. Koizumi, M. Yamada, J. Synchrotron Rad. 17 (2010) 530–539.

[99] A. Urakawa, T. Bürgi, A. Baiker, Chem. Eng. Sci. 63 (2008) 4902–4909.

[100] A.I. Dugulan, J.A.R. van Veen, E.J.M. Hensen, Appl. Catal. B Environ. 142–143 (2013) 178–186.

[101] A.I. Dugulan, E.J.M. Hensen, J.A.R. van Veen, Catal. Today 130 (2008) 126–134.

[102] O.İ. Şenol, E.-M. Ryymin, T.-R. Viljava, A.O.I. Krause, J. Mol. Catal. A Chem. 268 (2007) 1–8.